Signals of Nonturbulent Motions Caused by Stable Stratification in Near-Surface Sonic Anemometer Data

YING PAN,[a] SAMUEL C. WRAY,[a] AND EDWARD G. PATTON[b]

[a] *The Pennsylvania State University, University Park, Pennsylvania*
[b] *NSF National Center for Atmospheric Research, Boulder, Colorado*

(Manuscript received 17 April 2024, in final form 24 December 2024, accepted 24 February 2025)

ABSTRACT: Understanding the interactions between turbulent and nonturbulent motions has been a persistent challenge faced by the community studying stably stratified turbulent flows. For flows with high Reynolds number, high Rossby number, and stable stratifications, nonturbulent motions involve physical mechanisms acting against instability development. Because turbulent motions are generated through an energy cascade via instability development, the presence of nonturbulent motions is expected to modify the energy distribution across scales compared to that of solely turbulent motions. The objective of this work is to identify in field data statistical signals of nonturbulent motions caused by stable stratification. The need to resolve energy-containing motions in both space and time requires high-frequency time series of velocity fluctuations collected using arrays of sonic anemometers. The analysis is performed using data from the Canopy Horizontal Array Turbulence Study (CHATS), during which a total of 31 sonic anemometers were deployed on a horizontal array and on a 30-m tower. Compared to other field campaigns which were also equipped with arrays of sonic anemometers, CHATS took an important advantage of already published nighttime canopy-scale waves derived from aerosol backscatter lidar images. After precluding complexities caused by nonstationarity and horizontal heterogeneity, signals of nonturbulent motions caused by stable stratification are identified from spatial autocorrelations of time-block-averaged velocity fluctuations. These signals are interpreted using existing understanding of turbulent canopy flows and two-dimensional Kelvin–Helmholtz instability development. The associated estimates of critical wavelengths and buoyancy periods agree well with the overall properties of nighttime canopy-scale waves derived from lidar images.

SIGNIFICANCE STATEMENT: This work investigates statistical signals of nonturbulent motions caused by stable stratification in sonic anemometer measurements of near-surface atmospheric flows. The detected signals of nonturbulent motions agree with theoretical predictions of the impacts of stable stratification on turbulent canopy flows. This agreement suggests potential advantages for understanding stably stratified near-surface flows using canopy-resolving simulations. The automatic, objective, statistical detection procedures, as well as the intermediate products of the periods of statistically stationary, horizontally homogeneous, approximately two-dimensional mean flows, are useful for improving the understanding of canopy flows for various stability conditions.

KEYWORDS: Gravity waves; Kelvin-Helmholtz instabilities; Turbulence; Boundary layer; In situ atmospheric observations; Time series

1. Introduction

Understanding the interactions between turbulent and nonturbulent motions has been a persistent challenge faced by the community studying stably stratified turbulent flows (Mahrt 2014; Sun et al. 2015). Turbulence-resolving large-eddy simulation (LES) has become an extremely useful tool to study such three-dimensional (3D) interactions (e.g., Lloyd et al. 2022), but the validation of atmospheric LES of stably stratified flows against field data is limited to mean profiles (e.g., Beare et al. 2006), coherent structures (e.g., Sullivan et al. 2016), and spatially filtered fluxes (e.g., McWilliams et al. 2023). The inability of the community to separate turbulent and nonturbulent motions in field data, which may be due to potentially overlapping time scales, a lack of physical basis, and complexities created by nonstationarity and horizontal heterogeneity [see reviews by Mahrt (2014), LeMone et al. (2019)], complicates observational intercomparison with atmospheric LES.

Consider flows with high Reynolds number, high Rossby number, and stable stratification. Riley and Lelong (2000) suggested partitioning flow perturbations into turbulence, with nonpropagating potential vorticity (PV) modes, and with propagating wave modes. The latter two modes, being nonturbulent motions, were lumped into a term called "submeso" by Mahrt (2014). Although the term submeso has been adopted by recent studies of stable boundary layers (e.g., Vercauteren et al. 2016), we choose not to use this term to avoid making implicit assumptions of the scales of nonturbulent motions.

Supplemental information related to this paper is available at the Journals Online website: https://doi.org/10.1175/JAS-D-24-0070.s1.

Wray's current affiliation: National Weather Service, Wakefield, Virginia.

Corresponding author: Ying Pan, yyp5033@psu.edu

DOI: 10.1175/JAS-D-24-0070.1

Instead, we seek for common characteristics of nonturbulent motions by revisiting the physical mechanisms associated with PV and wave modes. The PV modes refer to primarily horizontal flows with significant vertical vorticity, which can be approximated as horizontal advection of rotation around a vertical axis. The waves are actions occurring under restoring forces. Both rotation around a vertical axis and restoring forces are mechanisms acting against instability development. On the other hand, turbulence is generated through an energy cascade via instability development (Davidson 2015, chapter 1.4). Thus, one can potentially separate turbulent and nonturbulent motions according to the status of instability development and the associated energy cascade.

Given the above rationales, the presence of nonturbulent motions is expected to modify the energy distribution across scales compared to that of solely turbulent motions. Previous studies used cospectra [multiresolution (Vickers and Mahrt 2003, 2006b) or Fourier (French et al. 2007; Cook and Renfrew 2015; Zou et al. 2017)] to investigate the energy distribution across scales and potential signals of nonturbulent motions. However, these studies used a different separation between turbulent and nonturbulent motions. They hypothesized that turbulent fluxes were directly related to local mean gradients while nonturbulent fluxes were relatively random and erratic (Vickers and Mahrt 2003). Under such hypothesis, solely turbulent motions were expected to present cumulative integrals of cospectra that would vary monotonically with increasing time scale [e.g., Fig. 4 in Vickers and Mahrt (2003) and Fig. 2 in Zou et al. (2017)], while nonmonotonic variations were considered as signals of nonturbulent motions. Unsurprisingly, linking such cospectra behaviors to nonturbulent motions becomes questionable when a local flux–gradient relationship becomes invalid due to nonlocal transport by organized large-scale turbulent motions such as convective eddies on atmospheric boundary layer (ABL) scales (Vickers and Mahrt 2003; French et al. 2007). Whether any behaviors of cospectra can be used to separate turbulent and nonturbulent motions based on the status of instability development remains unknown.

The objective of this work is to identify in field data statistical signals of nonturbulent motions caused by stable stratification, which provides restoring forces acting against instability development. Three major steps are needed to achieve this objective. The first step is to limit the cause of nonturbulent motions to only stable stratification by precluding complexities caused by nonstationarity and horizontal heterogeneity. Note that PV modes are also excluded upon completing this step, meaning that only waves are considered as possible nonturbulent motions. The second step is to compare the energy distribution across scales during two subsets of the resulting periods, one with unstable stratification to represent solely turbulent motions and the other with stable stratification to represent a mixture of turbulent and nonturbulent motions. This approach of separating periods is appropriate for flow fields controlled by only mean shear and stratification. For statically unstable conditions, both shear and stratification contribute to instability development, and therefore, solely turbulent motions are expected. For statically stable conditions, stratification suppresses the growth of instabilities generated by shear, and therefore, a mixture of turbulence and possible internal gravity waves is expected. The difference in energy distribution between these two subsets of periods is considered as signals of nonturbulent motions caused by stable stratification. Because quantifying the energy distribution across scales requires resolving energy-containing motions in both space and time, the preferred data are high-frequency time series of velocity fluctuations collected using arrays of sonic anemometers. This data preference narrows down the scope of this work to near-surface flows. The last step is to verify whether the obtained signals of nonturbulent motions caused by stable stratification are consistent with theoretical understanding and evidence from contemporary data collected using other instruments.

The subsequent sections of this paper are organized as follows. Section 2 selects the field observational data and describes the analysis procedures. Section 3 presents results in two parts: 1) discusses the identified periods of statistically stationary and horizontally homogeneous mean flows and 2) discusses the statistical signals of nonturbulent motions caused by stable stratification in comparison with statistics of solely turbulent motions. Conclusions and implications for future LES of stable ABLs are given in section 4.

2. Field observational data and analysis procedures

a. Selection of field observational data

We select the field observational dataset according to the objective of identifying statistical signals of nonturbulent motions caused by stable stratification and the three major steps to achieve this objective. First, to obtain periods of horizontally homogeneous mean flows, the experimental site needs to be above flat terrain and horizontally homogeneous roughness elements. Second, to compare periods of solely turbulent motions to those involving internal gravity waves, the data collection needs to cover a wide range of both unstable and stable conditions. Third, to calculate statistics across energy-containing scales in both space and time, the sensor deployment needs to include spatial sampling at high frequency. Last, to examine the identified signals of nonturbulent motions, the experiment needs to collect evidence of near-surface internal gravity waves using other instruments. All four requirements were satisfied during the Canopy Horizontal Array Turbulence Study (CHATS; Patton et al. 2011; UCAR/NCAR–Earth Observing Laboratory 2011), during which a total of 31 Campbell Scientific CSAT3 sonic anemometers were deployed on a horizontal array and on a 30-m tower, and an aerosol backscatter lidar was also deployed (see Fig. 1). The already published nighttime canopy-scale wave dynamics derived from aerosol backscatter lidar data (Mayor 2017) are an important advantage of selecting CHATS, especially for evaluation purposes, compared to other field campaigns which were also equipped with arrays of sonic anemometers.

CHATS took place in an 800 m × 800 m walnut orchard field in Dixon, California, during March–June 2007. In a nearly flat and horizontally homogeneous terrain, the orchard

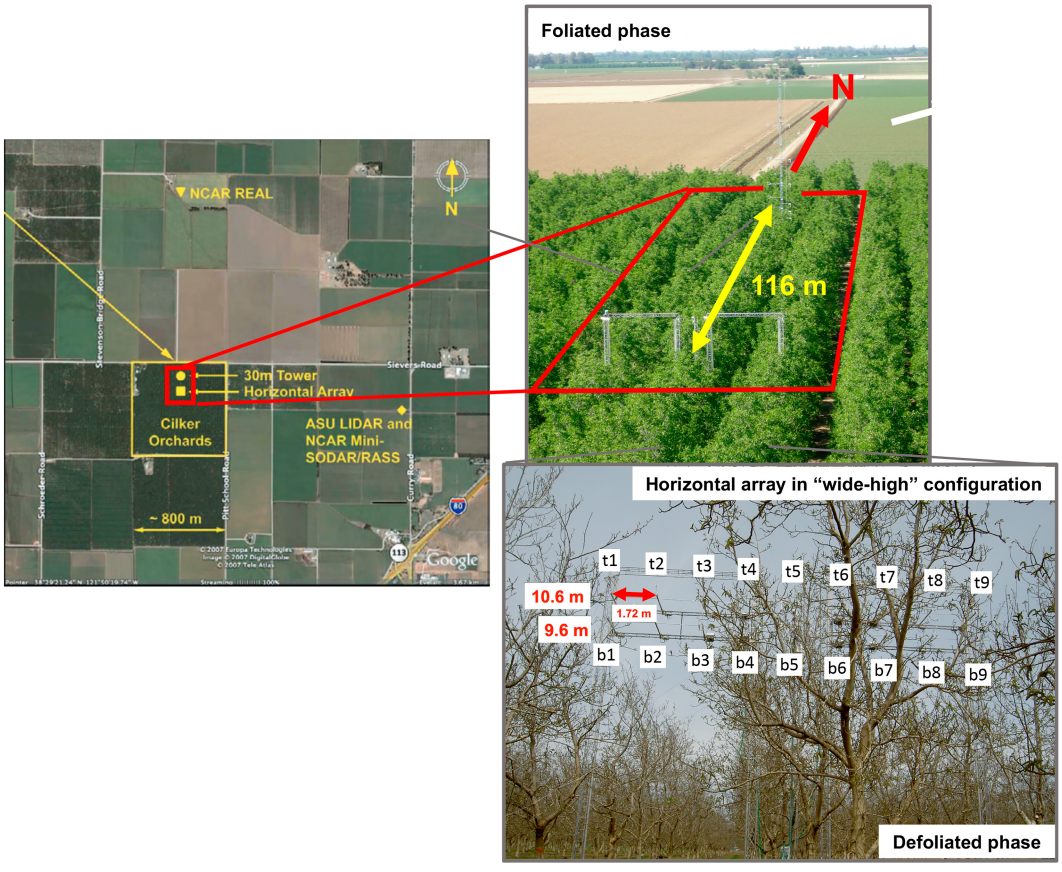

FIG. 1. Sensor deployment during CHATS: (left) the experimental site [map adopted from Patton et al. (2011)], (top right) the 30-m tower located at 116 m north of the horizontal array (photo taken during the foliated phase), and (bottom right) the horizontal array in the wide–high configuration with CSAT3 sonic anemometers t1–t9 on the top beam and b1–b9 on the bottom beam (photo taken during the defoliated phase). The aerosol backscatter lidar annotated as "NCAR REAL" was located 1.61 km north of the 30-m tower (Mayor 2010).

trees were approximately 10-m tall and spaced approximately every 7 m in both zonal (i.e., west–east) and meridional (i.e., south–north) directions. During CHATS, the stability parameter at canopy top ($h/\mathscr{L}$, where $h = 10$ m is the canopy height and $\mathscr{L}$ is the Obukhov length) ranged from below –0.2 to above 0.6 [reported by Dupont and Patton (2012), i.e., sufficiently wide]. A 30-m tower was located near the northernmost border of the orchard field, and a horizontal array was located 116 m south of the tower. The tower and the array center were located within the same row of trees. A total of 13 sonic anemometers were deployed facing west on the tower, at heights of 1.5, 3, 4.5, 6, 7.5, 9, 10, 11, 12.5, 14, 18, 23, and 29 m. Another 18 sonic anemometers were deployed facing south on the array that consisted of two horizontal beams separated vertically by 1 m. The height of the top beam was 3 m during the "low configuration" periods, 5.9 m during the "middle configuration" periods, and 10.6 m during the "high configuration" periods. On each of the beams, nine sonic anemometers were mounted and spaced equally in the zonal direction. The zonal spacing between two adjacent sensors was 0.5 m during the "narrow configuration" periods and 1.72 m during the "wide configuration" periods. All 31 CSAT3 sonic anemometers were operated at a frequency of 60 Hz sampling three velocity components and virtual temperature. For mean wind directions between 90° and 270° (hereafter referred to as "southerly mean wind"), the orchard canopy fetch was considered as ample for most of the sonic anemometers, except perhaps for the uppermost sensors on the tower during the most stably stratified periods (Patton et al. 2011). When interpreting CHATS data, one needs to be aware that the horizontal spatial correlations of flow properties measured by these sonic anemometers may not vanish with increasing averaging time owing to the spatially organized tree distribution (i.e., dispersive motions; Raupach and Shaw 1982).

Of the various CHATS array configurations, the "wide–high configuration" is most suitable for investigating statistical signals of nonturbulent motions caused by stable stratification. The high configuration is selected because the influences of a stable stratification are likely the strongest near the canopy top, as suggested by CHATS data showing that absolute heat flux values increase with increasing height within the canopy (Dupont and Patton 2012). Other forest observational data also show that nighttime wavelike motions are most clear

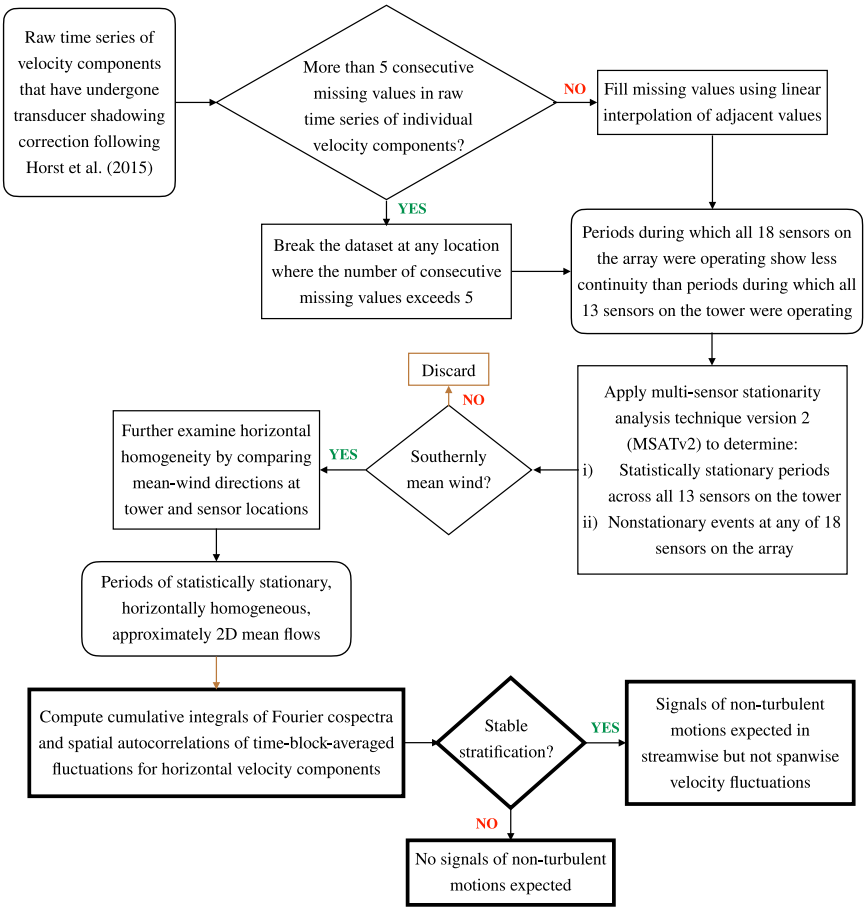

FIG. 2. A summary of data analysis procedures. The first stage (in boxes with thin boarder lines) is described in detail in appendix A. The second stage (in boxes with thick boarder lines) is the focus of the current section 2b.

near the canopy top (e.g., visually inspected by Lee 1997). The wide configuration is selected to maximize the range of available sensor separation in horizontal directions. CHATS consisted of a defoliated phase (15 March–13 April, before leaf-out) and a foliated phase (13 May–12 June, after leaf-out). The wide–high configuration periods took place between 0300 UTC 1 April and 1755 UTC 4 April during the defoliated phase and between 0000 UTC 13 May and 1609 UTC 17 May during the foliated phase.

b. *Analysis procedures*

Figure 2 summarizes the data analysis procedures, which can be separated into two major stages: (i) identifying periods of statistically stationary, horizontally homogeneous, approximately two-dimensional (2D) mean flows, and (ii) calculating velocity statistics and examining whether they capture signals of nonturbulent motions caused by stable stratification. The first stage relies on application of a flow-dependent, multi-sensor stationarity analysis technique version 2 [MSATv2; developed by Pan and Patton (2020)], whose procedures are described in detail in appendix A. The second stage (annotated using thick box lines in Fig. 2) is the focus of this subsection. Specifically, what statistics of what velocity components in what coordinate system should we investigate?

1) COORDINATE SYSTEM CHOICE

The behaviors of approximately 2D near-surface flows are preferred to be investigated in a coordinate system that aligns with the mean wind owing to horizontal anisotropy induced by mean shear. In reality, near-surface mean flows are never perfectly 2D, and time-averaged statistics near the canopy top are not fully exempted from dispersive motions (Raupach and Shaw 1982). Therefore, a perfect definition of the mean wind direction across all sensor locations is unavailable. Instead of debating what combination of data collected using what groups of sensors yields the best definition, we need only a practically appropriate estimate of the mean wind direction that does not lead to incorrect interpretation of results. In this work, we estimate the mean wind direction using data collected by the sensor at the canopy top on the 30-m tower and then examine the appropriateness of such choice by investigating the influence of associated uncertainties on major conclusions (see discussion in section 4a).

2) VELOCITY COMPONENTS OF INTEREST

In a stably stratified shear flow, buoyancy acts against the role of shear in amplifying a vertical displacement of an air parcel and therefore directly affects distribution of energy carried by vertical velocity fluctuations (w'). However, measurements of w' are highly sensitive to possible sonic tilts, whose correction angles cannot be estimated accurately [e.g., sensitive to averaging time scales, as reported by Vickers and Mahrt (2006a)]. The uncertainties associated with sonic tilts can be substantially reduced if statistics of horizontal velocity fluctuations are capable of capturing the influence of stable stratification. Under assumptions that the flow is Boussinesq, statistically stationary, horizontally homogeneous, and of large Reynolds and Rossby numbers, the Reynolds-averaged momentum equations in a mean wind coordinate system become (see the original Boussinesq equations in Pan and Patton (2017), their section 3a)

$$\frac{\partial \overline{u'w'}}{\partial z} = -\frac{1}{\rho_0}\frac{\partial \overline{p}}{\partial x} + \overline{f_x}, \tag{1}$$

$$\overline{v'w'} = 0, \tag{2}$$

$$\frac{\partial}{\partial z}\left(\frac{\partial \overline{p}}{\partial x}\right) = 0. \tag{3}$$

Here u, v, and w are the velocity components in streamwise (x), spanwise (y), and vertical (z) directions, respectively, ρ_0 is the hydrostatic air density, p is the pressure perturbation with respect to its hydrostatic state, and f_x is a force term representing both the form and viscous drag exerted by canopy elements on the flow. An overbar represents the Reynolds average (also known as an ensemble average), which—under the ergodic hypothesis—can be approximated using time averages over a sufficiently long statistically stationary period. A prime ($'$) represents fluctuation with respect to Reynolds-averaged values. The combination of (1) and (3) suggests negative $\overline{u'w'}$ at the canopy top, meaning that u' and w' are negatively correlated. This negative correlation is also supported by previous observations of approximately 180° phase angle differences between u' and w' in nighttime wavelike motions above forest canopy [see Fig. 5 in Lee (1997)]. Thus, one should expect signals of nonturbulent motions caused by stable stratification in u' statistics as well as in w' statistics. On the other hand, (2) suggests that v' and w' are uncorrelated, implying that v' statistics are not expected to contain signals of nonturbulent motions produced by stable stratification. Such expectations are supported by aerosol backscatter lidar data collected during CHATS, which suggest that nighttime wavelike motions near the canopy top propagate along mean wind directions (Mayor 2017). In summary, a statistical measure capable of capturing nonturbulent motions caused by stable stratification is expected to show unique behaviors for u', but not for v', under stable conditions compared to their behaviors under unstable conditions.

3) STATISTICS OF INTEREST

The role of nonturbulent motions in modifying the energy distribution across scales implies that their characteristic scales are likely different from those of solely turbulent motions. For turbulence, motions on the integral length scale are characterized by the integral time scale, while motions on increasingly small length scales are characterized by increasingly small time scales. In the presence of stable stratification, motions on length scales heavily influenced by the stratification should be characterized by the period of internal gravity waves. To capture this change in the space–time relationships, we need statistics carrying both spatial and temporal information. Knowing that the characteristic scales influence both covariance and coherence, we propose to investigate two candidates defined below: (i) the cumulative integrals of Fourier cospectra of fluctuations at separated locations and (ii) the spatial autocorrelations of time-block-averaged fluctuations.

(i) Cumulative integrals of Fourier cospectra

Given a horizontal separation ($\mathbf{r}$) in a horizontally homogeneous flow, two-point statistics become independent of the horizontal location ($\mathbf{x}$). The Fourier cospectrum, $\mathrm{Co}_{\phi\phi}(\mathbf{r}; f)$, represents the contributions of motions at frequency f to the covariance, $\overline{\phi'(\mathbf{x}, t)\phi'(\mathbf{x}+\mathbf{r}, t)}$, where ϕ is an arbitrary flow variable and t is the time. Here, an overbar represents an ensemble average, and a superscript prime represents a fluctuation with respect to the ensemble-averaged value. Practically, $\mathrm{Co}_{\phi\phi}(\mathbf{r}; f)$ plotted against f on a logarithmic scale consists of strongly scattered data points at the high-frequency end. With frequency-smoothing embedded, the cumulative integral

$$O_{\phi\phi}(\mathbf{r}; f) = \int_{\infty}^{f} \mathrm{Co}_{\phi\phi}(\mathbf{r}; f_*)df_* \tag{4}$$

provides convenient visual inspection of the contribution of motions at frequencies of f or larger to the two-point covariance (Oncley et al. 1996). Note that $\overline{\phi'(\mathbf{x}, t)\phi'(\mathbf{x}+\mathbf{r}, t)}$ can also be called a correlation and $O_{\phi\phi}(\mathbf{r}; f)$ can also be called the ogive of correlations.

(ii) Spatial autocorrelations of time-block-averaged fluctuations

Averaging a flow variable ϕ over time blocks of Δt yields

$$\tilde{\phi}(\mathbf{x}, t; \Delta t) = \frac{1}{\Delta t}\int_{t}^{t+\Delta t} \phi dt, \tag{5}$$

where $t = 0, \Delta t, 2\Delta t, \ldots, \mathscr{T} - \Delta t$ and $\mathscr{T}$ is the duration of a statistically stationary period. The fluctuation $\phi''(\mathbf{x}, t; \Delta t) = \tilde{\phi}(\mathbf{x}, t; \Delta t) - \overline{\phi}(\mathbf{x})$ represents the contribution of motions on time scales of Δt and larger to the total fluctuation $\phi'(\mathbf{x}, t; \Delta t) = \phi(\mathbf{x}, t) - \overline{\phi}(\mathbf{x})$. Given a horizontal separation ($\mathbf{r}$) in a horizontally homogeneous flow, the spatial autocorrelation of time-block-averaged fluctuations is defined as

$$R_{\phi\phi}(\mathbf{r}; \Delta t) = \frac{\overline{\phi''(\mathbf{x}, t; \Delta t)\phi''(\mathbf{x}+\mathbf{r}, t; \Delta t)}}{\sigma_{\phi}(\mathbf{x}; \Delta t)\sigma_{\phi}(\mathbf{x}+\mathbf{r}; \Delta t)}, \tag{6}$$

where the standard deviation of time-block-averaged fluctuations at a single location is defined as

$$\sigma_{\phi}(\mathbf{x}; \Delta t) = [\overline{\phi''(\mathbf{x}, t; \Delta t)\phi''(\mathbf{x}, t; \Delta t)}]^{1/2}. \tag{7}$$

TABLE 1. Stationary south-wind periods determined using tower data during CHATS' defoliated phase with wide–high configuration, by applying MSATv2 to two continuous data-collecting periods: (i) from 2212 UTC 31 Mar to 0121 UTC 3 Apr and (ii) from 0124 UTC 3 Apr to 1651 UTC 5 Apr. Periods D.a–D.e are determined using $\delta t = 3$ min with $\alpha = 0.25$, while periods D.f–D.h are determined using $\delta t = 6$ min with $\alpha = 0.40$. This table is adopted from Pan and Patton (2020), with necessary modifications to show statistics of interested in this work. For each period, a time average over the entire duration is used to approximate ensemble average. All statistics are computed at the canopy top ($z/h = 1$, where $h = 10$ m is the canopy height). The friction velocity is given by $u_* = [(\overline{u'w'})^2 + (\overline{v'w'})^2]^{1/4}$. The stability regimes are defined following Dupont and Patton (2012): free convection (FrC, $-20 \le h/\mathcal{L} < -0.2$), forced convection (FoC, $-0.2 \le h/\mathcal{L} < -0.01$), near neutral (NN, $-0.01 \le h/\mathcal{L} < 0.02$), transition to stable (TS, $0.02 \le h/\mathcal{L} < 0.6$), and stable (S, $0.6 \le h/\mathcal{L} < 20$). Here, $\mathcal{L} = u_*^3/[\kappa(g/\theta)\overline{w'\theta'}]$ is the Obukhov length, $\kappa = 0.4$ is the von Kármán constant, $g = 9.81$ m s^{-2} is the gravitational acceleration, and θ is the virtual potential temperature.

Period	Time	No. of stationary intervals	Mean wind speed $\overline{u}_h$ (m s^{-1})	Mean wind direction (°)	Friction velocity u_* (m s^{-1})	Stability parameter $h/\mathcal{L}$	Stability regime	Nonstationary event at array location	$e_{\overline{u'u'}}$	$e_{\overline{v'v'}}$	$\Delta t_{c,u}$ (s)	$\Delta t_{c,v}$ (s)
D.a	1700–1742 UTC 1 Apr	1	1.4	140.9	0.32	−0.498	FrC	Unknown	0.11	0.29	180	120
D.b	1757–1836 UTC 1 Apr	1	1.0	162.6	0.28	−0.993	FrC	Unknown	0.13	0.12	117	156
D.c	0003–0100 UTC 2 Apr	7	2.7	217.8	0.74	−0.044	FoC	Yes	0.06	0.13	171	47.5
D.d	0018–0051 4 Apr	1	2.4	196.7	0.62	−0.059	FoC	No	0.12	0.18	79.2	110
D.e	0642–0721 UTC 4 Apr	1	2.2	198.6	0.45	0.016	NN	No	0.08	0.15	97.5	292.5
D.f	2230 UTC 31 Mar–0018 UTC 1 Apr	2	3.1	209.8	0.72	−0.057	FoC	Unknown	0.04	0.05	180	1296
D.g	2048–2248 1 Apr	1	1.1	179.5	0.39	−0.438	FrC	No	0.12	0.16	400	480
D.h	2106–2342 UTC 3 Apr	5	1.6	190.6	0.54	−0.232	FrC	No	0.08	0.11	468	520

Physically, $R_{\phi\phi}(\mathbf{r}; \Delta t)$ represents the contribution of motions at a time scale Δt and larger to the coherence of fluctuations at two points.

3. Results

a. *Periods of statistically stationary, horizontally homogeneous, approximately 2D mean flows*

In this subsection, we present results from the first stage of the analysis procedures. As shown in Fig. 2, this stage consists of four key steps: (i) identifying periods with stationary mean wind across all 13 heights on the 30-m tower, (ii) examining the presence of nonstationary events across all 18 sensors on the horizontal array, (iii) selecting only periods with southerly mean wind (i.e., winds from between 90° and 270°, see section 2a), and (iv) retaining periods with approximately 2D mean wind field. With the mean wind direction estimated using data collected by the sensor at the canopy top on the tower [see section 2b(1)], one can switch the sequence of steps ii and iii. Here, we first show results of stationary periods identified at the tower location associated with southerly mean wind (i.e., by completing steps i and iii) and then examine each of these periods for nonstationary events at the array location (i.e., step ii) and the spatial variations of mean wind directions (i.e., step iv).

To determine stationary periods using MSATv2 (see detailed explanation in appendix A), one needs to optimize key parameters for the specific scientific question of interest. In this work, it is desirable for the stationary periods to cover a wide range of stability conditions (as one of the four criteria of selecting field observational data) with southerly mean winds (to guarantee ample fetch of the orchard canopy during CHATS). These requirements are consistent with those in Pan and Patton (2020), whose parameter optimization strategy was as follows: Given an averaging time block (δt) used to obtain MSATv2 inputs, an optimal choice of the significance level (α) for the reverse arrangement test (RAT; Kendall et al. 1979) should yield a maximum number of reliable stationary periods associated with southerly mean winds (referred to as "stationary south-wind periods"). The same strategy of optimizing δt and α is used here.

Table 1 shows stationary south-wind periods identified by Pan and Patton (2020) using tower data during CHATS' defoliated phase with wide-high configuration. Employing $\delta t = 3$ min yields a maximum of five stationary south-wind periods with $\alpha = 0.25$ (D.a–D.e), while employing $\delta t = 6$ min yields a maximum of three stationary south-wind periods with $\alpha = 0.40$ (D.f–D.h). Similar analysis is now conducted using tower data during CHATS' foliated phase with wide-high configuration. Employing $\delta t = 3$ min yields a maximum of 12 stationary south-wind periods with $\alpha = 0.15$, while employing $\delta t = 6$ min yields a maximum of eight stationary south-wind periods with $\alpha = 0.15$ (Table 2). Among these stationary south-wind periods found in the tower data, applying MSATv2 to the array data identifies nonstationary events during periods D.c and F.i. As explained in appendix B, these nonstationary events occurring at the array location while the flow at the tower location is deemed stationary appear like the tails of associated dynamic transitions.

Before moving on to the last step of examining mean wind directions, we need to explain why optimal α values for a given δt are obtained separately for defoliated and foliated phases. The substantially different climatological and canopy structure conditions between early April and mid-May suggest that enforcing a uniform optimal α value for both periods is potentially inappropriate. First, no rain occurred during 28 March–8 April while irrigation did not start until 13 April, suggesting that the soil was rather dry during early April. On the contrary, a number of rain events occurred during 9–22 April and irrigation was performed during 16–18 May, suggesting that the soil was relatively wet during mid-May.

TABLE 2. As in Table 1, but for stationary south-wind periods determined using tower data during CHATS' foliated phase with wide–high configuration, by applying MSATv2 to three continuous data-collecting periods: (i) from 2233 UTC 13 May to 1900 UTC 14 May, (ii) from 2000 UTC 14 May to 1839 UTC 15 May, and (iii) from 1842 UTC 15 May to 1827 UTC 17 May. Periods F.a–F.l are determined using $\delta t = 3$ min with $\alpha = 0.15$, while periods F.m–F.t are determined using $\delta t = 6$ min with $\alpha = 0.15$.

Period	Time	No. of stationary intervals	Mean wind speed $\overline{u}_h$ (m s^{-1})	Mean wind direction (°)	Friction velocity u_* (m s^{-1})	Stability parameter $h/\mathcal{L}$	Stability regime	Nonstationary event at array location	$e_{\overline{u'u'}}$	$e_{\overline{v'v'}}$	$\Delta t_{c,u}$ (s)	$\Delta t_{c,v}$ (s)
F.a	0736–0812 UTC 15 May	1	1.2	185.9	0.37	0.074	TS	Unknown	0.06	0.05	54	54
F.b	1842–1915 UTC 15 May	1	1.4	185.3	0.59	−0.101	FoC	No	0.14	0.09	26.4	41.3
F.c	2209–2303 UTC 15 May	4	1.8	198.4	0.73	−0.027	FoC	No	0.12	0.06	45	45
F.d	2354 15 May–0024 16 May	1	1.9	205.7	0.76	−0.009	NN	No	0.08	0.06	45	33.3
F.e	0024–0106 UTC 16 May	2	2.0	201.7	0.86	−0.022	FoC	No	0.06	0.06	60	23.3
F.f	0109–0151 UTC 16 May	3	2.3	197.2	0.89	−0.006	NN	No	0.06	0.06	56	26.3
F.g	0221–0342 UTC 16 May	4	2.4	204.6	0.86	0.007	NN	No	0.04	0.04	97.2	36
F.h	0354–0424 UTC 16 May	1	2.2	197.4	0.78	0.009	NN	No	0.05	0.05	40	24
F.i	0600–0630 UTC 16 May	1	1.3	190.2	0.39	0.069	TS	Yes	0.07	0.05	60	30
F.j	0106–0139 UTC 17 May	1	1.4	181.7	0.56	0.010	NN	No	0.10	0.07	45	33
F.k	0300–0342 UTC 17 May	1	1.6	193.4	0.51	0.050	TS	No	0.05	0.06	52.5	21
F.l	0533–0609 UTC 17 May	3	1.2	187.2	0.38	0.074	TS	No	0.05	0.06	52.5	26.25
F.m	0654—0806 UTC 15 May	1	1.2	186.1	0.36	0.084	TS	Unknown	0.04	0.04	90	67.5
F.n	1536–1748 UTC 15 May	22	0.7	211.7	0.36	−0.313	FrC	Unknown	0.07	0.11	396	247.5
F.o	1854–2024 UTC 15 May	5	1.6	185.0	0.67	−0.084	FoC	No	0.06	0.06	108	112.5
F.p	2212–2312 UTC 15 May	1	1.9	199.1	0.72	−0.026	FoC	No	0.10	0.06	72	45
F.q	2318 UTC 15 May–0030 UTC 16 May	1	2.0	205.0	0.77	−0.011	FoC	No	0.04	0.04	108	54
F.r	0218–0336 UTC 16 May	3	2.4	204.5	0.86	0.007	NN	No	0.05	0.04	78	36
F.s	0606–0724 UTC 16 May	1	1.1	186.4	0.37	0.073	TS	No	0.05	0.04	97.5	173.3
F.t	0700–0930 UTC 17 May	1	1.1	185.0	0.36	0.087	TS	No	0.03	0.03	450	562.5

An increase in soil moisture implies a reduction in Bowen ratio (i.e., decrease in sensible and increase in latent heat flux). Second, the presence of leaves may further decrease the Bowen ratio through transpiration, causing a reduction in buoyancy-dominated stability conditions in mid-May compared to early April. Third, the presence of leaves may also increase the bulk drag coefficient (defined as $u_*^2/\overline{u}_h^2$) and therefore increase the canopy-top mean shear for a given mean wind speed, producing more shear-dominated stability conditions. Here, values of friction velocity (u_*) and canopy-top mean wind speed ($\overline{u}_h$, where $h = 10$ m is the canopy height) are presented in Tables 1 and 2. Results obtained during stationary south-wind periods for near-neutral (NN) conditions suggest that $u_*^2/\overline{u}_h^2$ estimates increase from 0.04 during the defoliated phase to 0.12–0.16 during the foliated phase. Last, the reduction in buoyancy-dominated stability conditions and the increase in shear-dominated stability conditions are also evident from the dominant stability regimes associated with stationary south-wind periods, which change from mostly free convection (FrC) and forced convection (FoC) during the defoliated phase (Table 1) to often NN and transition to stable (TS) during the foliated phase (Table 2).

We now perform the last step of this subsection: examining whether the mean wind field is approximately 2D during each stationary south-wind period. First of all, the Rossby number at the canopy top is on the order of 10^3 during each of the periods in Tables 1 and 2, consistent with the assumption made in section 2b(2) to ignore Coriolis force. To reduce the complexities caused by dispersive motions, we exclude data measured on the bottom beam of the array (i.e., right below the canopy top) from the comparison of mean wind directions at different horizontal locations. In other words, we only compare mean wind directions measured on the top beam of the array (i.e., right above the canopy top) and at the canopy top on the tower, where dispersive motions should be less prevalent. This comparison does not include periods D.f and F.a, during which data collections on the top beam of the array were discontinuous. Results presented in Table 3 show that D.b is the only period reporting substantial differences (>20°) in mean wind directions between array and tower locations. The apparently 3D mean flow during period D.b is also supported by Pan and Patton (2020) reporting large variation of mean wind directions with height at the tower location (which cannot be explained by Coriolis force given the Rossby number on the order of 10^3). During each of the other periods, the mean wind direction measured by each sensor on the top beam of the array differs from that measured by the canopy-top sensor on the tower by less than 8°, and therefore, the mean flow can be considered as approximately 2D. The weak variation of mean wind directions with height at the tower location (not shown here) further confirms that the mean flow during each of these periods is approximately 2D.

b. *Statistical signals of nonturbulent motions caused by stable stratification*

In this subsection, we calculate statistics that carry both spatial and temporal information using measurements of streamwise and spanwise velocity components. Applying the

TABLE 3. Differences between mean wind directions measured by each sensor on the top beam of the array (t1–t9 in Fig. 1) and that measured at the canopy top on the tower during each period in Tables 1 and 2 (except for periods D.f and F.a).

Period	t1	t2	t3	t4	t5	t6	t7	t8	t9
D.a	2.5	−0.1	1.6	1.3	0.7	−0.3	1.1	0.2	2.8
D.b	−25.7	−27.3	−27.5	−26.7	−39.2	−26.1	−23.8	−24.6	−21.2
D.c	−2.3	−4.7	−1.4	−1.1	−0.04	−0.9	−0.3	−2.9	−1.2
D.d	−1.0	−3.7	−1.6	−1.4	−0.5	−1.3	−0.4	−2.4	−1.0
D.e	1.5	−0.9	1.9	2.4	3.3	2.6	3.7	1.6	3.6
D.g	−7.0	−7.9	−7.9	−6.5	−5.5	−5.1	−3.3	−5.9	−3.5
D.h	2.5	0.5	2.0	3.1	4.7	5.2	6.0	3.5	4.8
F.b	0.1	−1.9	1.1	1.1	1.5	3.5	5.0	−0.7	3.0
F.c	3.3	2.0	2.2	2.7	5.0	4.7	4.9	1.3	4.7
F.d	6.8	5.5	6.6	5.8	7.7	6.6	5.8	2.4	5.9
F.e	3.5	2.7	3.3	3.1	5.9	5.0	5.4	1.9	5.7
F.f	2.7	2.2	3.2	4.3	6.2	4.6	5.1	2.4	5.8
F.g	1.8	2.1	1.7	1.8	4.8	2.2	2.5	−0.02	3.7
F.h	3.9	3.2	2.4	3.3	5.7	4.1	4.3	2.0	4.9
F.i	−0.8	0.3	0.7	0.9	3.0	1.4	2.2	−0.6	2.0
F.j	5.0	3.2	3.5	4.2	3.6	4.2	5.5	−1.0	2.8
F.k	2.0	2.4	1.6	1.9	3.7	1.8	3.5	1.7	5.7
F.l	−0.8	−0.2	−0.9	0.2	1.3	−0.5	0.8	−2.6	0.4
F.m	0.4	1.2	0.4	1.7	3.4	1.0	2.1	−0.7	2.8
F.n	4.9	−1.2	3.3	1.9	3.6	6.2	5.9	1.5	4.7
F.o	0.4	−2.0	−1.8	−0.9	−1.2	0.2	2.1	−3.4	−0.2
F.p	1.5	0.2	0.2	1.1	3.6	3.5	3.6	0.1	3.9
F.q	5.7	4.3	5.0	4.7	6.8	5.9	5.7	2.1	5.9
F.r	2.1	2.3	2.0	2.2	5.1	2.5	2.8	0.2	3.9
F.s	−0.7	0.3	−0.1	1.0	1.6	−0.9	0.3	−2.6	0.4
F.t	−0.6	0.01	−0.5	1.1	1.5	−0.3	0.8	−2.0	0.8

first statistical candidate to the data [i.e., cumulative integrals of Fourier cospectra of fluctuations at separated locations, defined in section 2b(3)(i)] reveals no unique behavior under stable conditions for either u or v compared to unstable conditions (see in the online supplemental material). These results indicate that nonturbulent motions caused by stable stratification are not identified by this technique and are therefore not shown here. Results from applying the second statistical candidate [the spatial autocorrelations of time-block-averaged fluctuations, defined in section 2b(3)(ii)] show unique behaviors under stable conditions for u, but not for v, compared to their behaviors under unstable conditions. These results are consistent with the anticipated signals of nonturbulent motions caused by stable stratification [explained in section 2b(2)] and are therefore discussed below in detail.

1) OBSERVING THE BEHAVIORS OF $R_{\phi\phi}(\mathbf{r}; \Delta t)$

Before interpreting results of $R_{\phi\phi}(\mathbf{r}; \Delta t)$, it is important to mention that these results are meaningful only when the denominator in (6), $\sigma_\phi(\mathbf{x}; \Delta t)\,\sigma_\phi(\mathbf{x}+\mathbf{r}; \Delta t)$, remains well above the uncertainty of estimating the variance, $\overline{\phi'\phi'}$. Using a time average to approximate, an ensemble average involves uncertainty caused by potentially biased samples of possible realizations, known as "random error" (Lumley and Panofsky 1964),

$$e_{\overline{\phi'\phi'}} = \frac{\sigma_{\phi'\phi'}}{\overline{\phi'\phi'}}\sqrt{\frac{2\tau_{\phi'\phi'}}{\mathcal{T}}}, \tag{8}$$

where $\tau_{\phi'\phi'}$ is the integral time scale of $\phi'\phi'$. Practically, we consider $R_{\phi\phi}(\mathbf{r}; \Delta t)$ estimates meaningful up to a critical averaging time block, $\Delta t_{c,\phi}$, at which $[\sigma_\phi(\mathbf{x}; \Delta t)]^2/\overline{\phi'\phi'}$ drops to twice of $e_{\overline{\phi'\phi'}}$. The values of $e_{\overline{u'u'}}$ and $e_{\overline{v'v'}}$ as well as the corresponding $\Delta t_{c,u}$ and $\Delta t_{c,v}$ are presented in Tables 1 and 2. Given a maximum of 562.5 s (≈10 min) across all $\Delta t_{c,u}$ and $\Delta t_{c,v}$ values, $R_{uu}(\mathbf{r}; \Delta t)$ and $R_{vv}(\mathbf{r}; \Delta t)$ results are calculated for each possible value of $\Delta t \le 10$ min that is (i) divisible by the sampling interval (1/60 s) and (ii) a factor of $\mathcal{T}$. These spatial autocorrelation results are presented in Figs. 3–6 that are organized by stability regimes. Given an $\mathbf{r}$ value, the dependence of $R_{uu}(\mathbf{r}; \Delta t)$ and $R_{vv}(\mathbf{r}; \Delta t)$ on Δt remains smooth at Δt smaller than integral time scales, but fluctuates strongly at Δt larger than integral time scales. The most profound fluctuations occur at $\Delta t > \Delta t_{c,\phi}$ (annotated by gray-shaded areas), confirming the necessity to focus on meaningful results at $\Delta t > \Delta t_{c,\phi}$.

With $\Delta t \to 0$, all values of $R_{vv}(\mathbf{r}; \Delta t)$ are positive or near zero, while some values of $R_{uu}(\mathbf{r}; \Delta t)$ can become more negative than −0.05 (referred as "statistically significantly negative"). With a positive value at $\Delta t \to 0$, the spatial autocorrelation increases with increasing Δt until approaching or exceeding $\Delta t_{c,\phi}$. With a statistically significant negative value at $\Delta t \to 0$, the spatial autocorrelation decreases with increasing Δt until reaching a minimum and then increases with increasing Δt. Because the statistically significant negative values occur for only $R_{uu}(\mathbf{r}; \Delta t)$ but not $R_{vv}(\mathbf{r}; \Delta t)$, we are particularly interested in the space–time relationships revealed by the

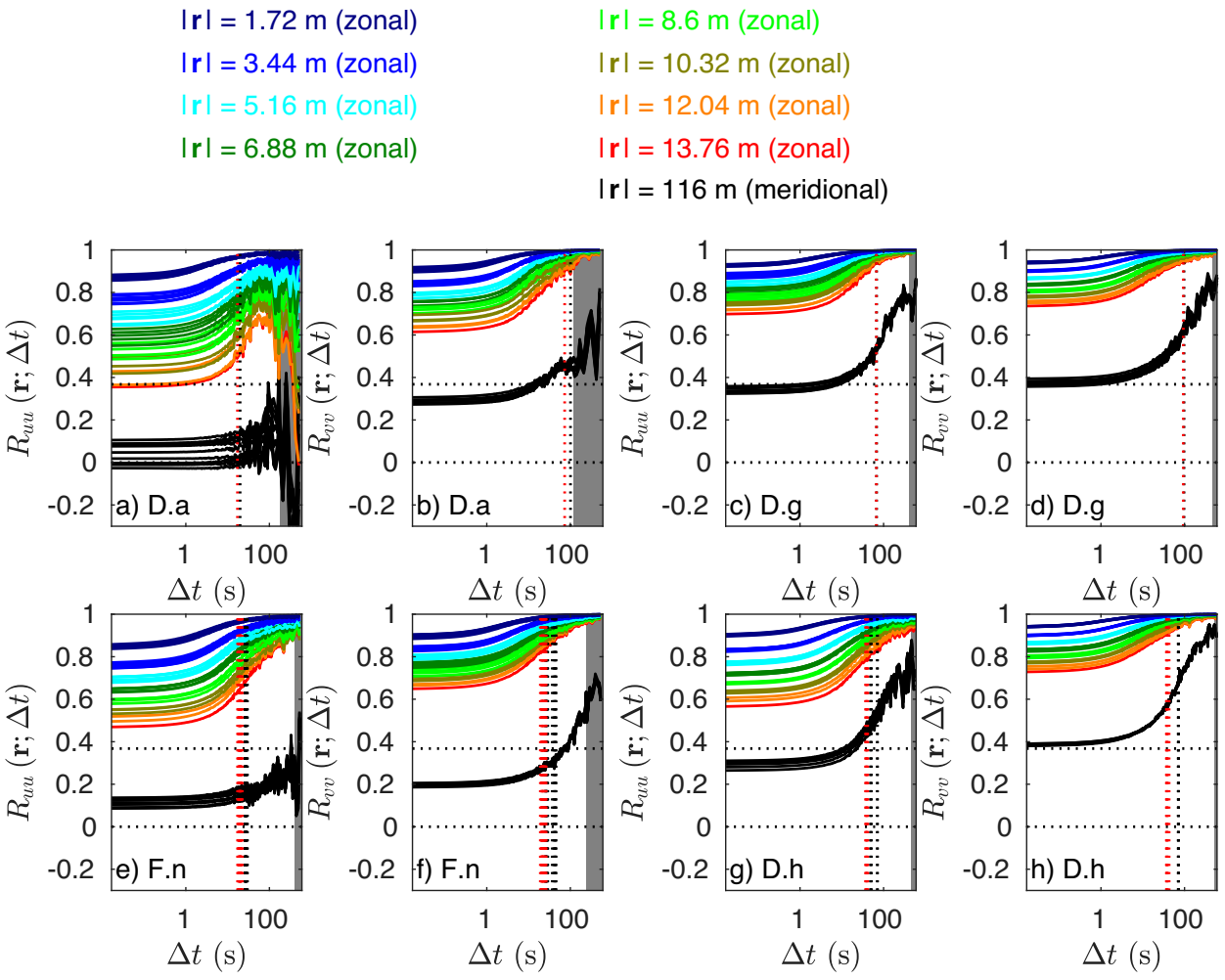

FIG. 3. (a)–(h) The spatial autocorrelations of time-block-averaged streamwise and spanwise velocity fluctuations [$R_{uu}(\mathbf{r};\Delta t)$ (odd columns) and $R_{vv}(\mathbf{r};\Delta t)$ (even columns), respectively] during FrC periods. Curves of various colors represent correlations between two sensors separated by various distances. The gray shaded areas annotate results calculated with $\Delta t > \Delta t_{c,\phi}$, which involve too large uncertainty considering the random error in velocity variance estimates for autocorrelation results to be meaningful. Horizontal dotted lines annotate correlation values of 0 and $1/e$, respectively. Vertical dotted lines represent integral time scales (τ) observed using the canopy-top tower sensor, estimated by identifying the e-folding time lag (red) and integrating the autocorrelation up to the first zero crossing (black). The number of red or black vertical dotted lines in each panel corresponds to *the number of stationary intervals* for each stationary period (provided in Tables 1 and 2). When red and black vertical dotted lines are collocated, only red vertical dotted lines at the front are visible [e.g., (c) and (d)].

associated nonmonotonic variation of $R_{uu}(\mathbf{r};\Delta t)$ with Δt and the potential connections to nonturbulent motions. At a meridional separation distance of 116 m (i.e., between the array and tower locations), $R_{uu}(\mathbf{r};\Delta t \to 0) < -0.05$ occurs only during period D.c (black solid curves in Fig. 4g), which is one of the two periods known for the presence of nonstationary events at the array location. Therefore, the unique behavior of $R_{uu}(\mathbf{r} = 116$ m meridional; $\Delta t)$ during period D.c is likely caused by nonstationarity rather than nonturbulent motions. At a zonal separation distance of 13.76 m (i.e., between sensors t1 and t9 on the array), $R_{uu}(\mathbf{r};\Delta t \to 0) < -0.05$ occurs during most periods characterized by $h/\mathscr{L} > 0$ (red solid lines in Figs. 5m and 6c,e,g,k). During the NN period D.e (Fig. 5m), $R_{uu}(\mathbf{r} = 13.76$ m zonal; $\Delta t)$ becomes increasingly negative until reaching a minimum at approximately the integral time scales. During TS periods (Fig. 6), $R_{uu}(\mathbf{r} = 13.76$ m zonal; $\Delta t)$ becomes increasingly negative until reaching a minimum at approximately half of a buoyancy period, which is typically an order of magnitude larger than integral time scales. Such substantial change of the behavior of $R_{uu}(\mathbf{r} = 13.76$ m zonal; $\Delta t)$ with stability conditions is unique, which may be signs of nonturbulent motions caused by stable stratification.

2) EXAMINING THE THEORETICAL BASE OF POTENTIAL SIGNALS OF NONTURBULENT MOTIONS

Because $R_{\phi\phi}(\mathbf{r};\Delta t)$ measures the coherence of flows, we examine the physical base of the nonturbulent motion signatures

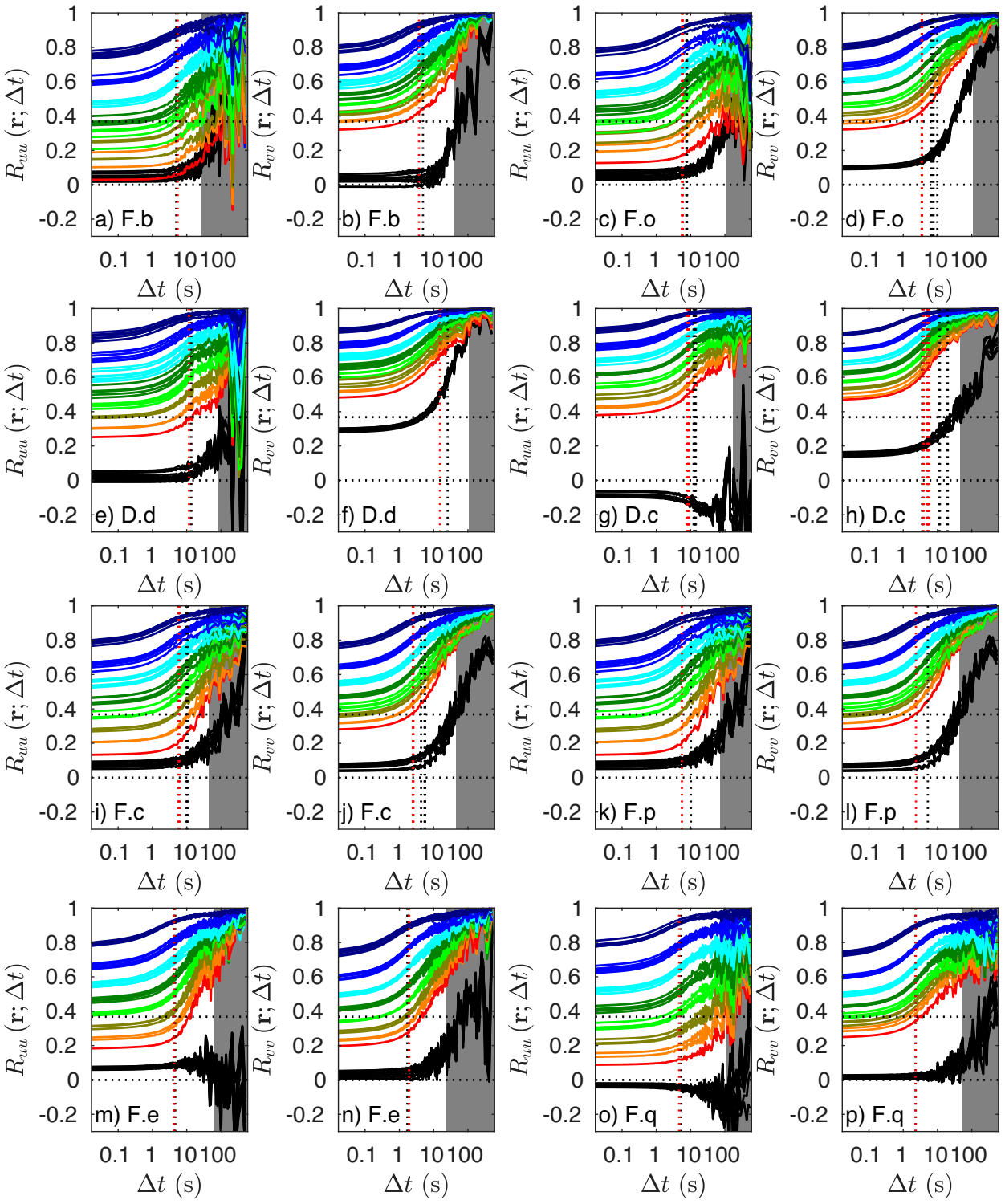

FIG. 4. The spatial autocorrelations of time-block-averaged streamwise and spanwise velocity fluctuations [$R_{uu}(\mathbf{r};\Delta t)$ (odd columns) and $R_{vv}(\mathbf{r};\Delta t)$ (even columns), respectively] during FoC periods. Refer to Fig. 3 for representation of lines and symbols.

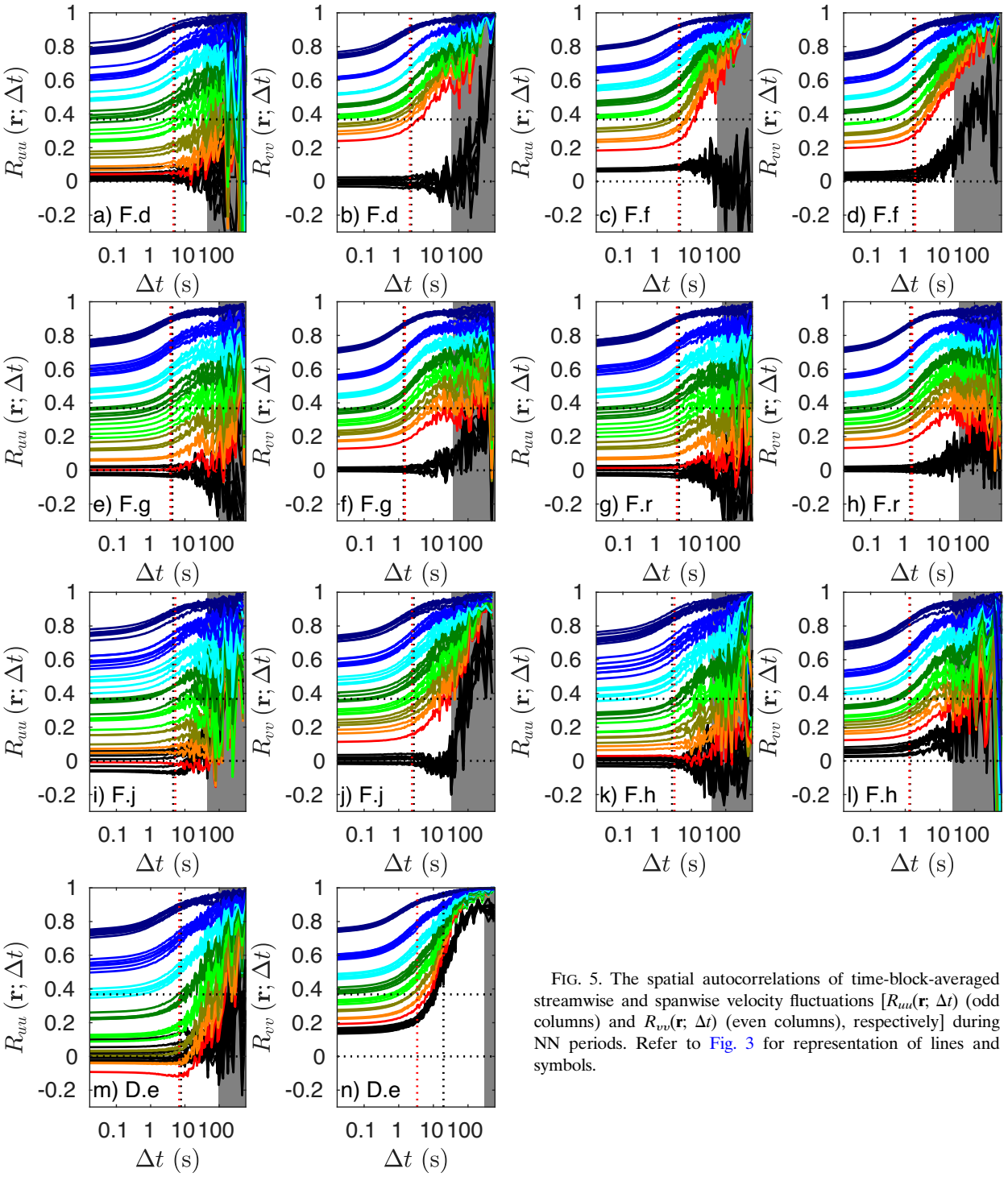

FIG. 5. The spatial autocorrelations of time-block-averaged streamwise and spanwise velocity fluctuations [$R_{uu}(\mathbf{r};\Delta t)$ (odd columns) and $R_{vv}(\mathbf{r};\Delta t)$ (even columns), respectively] during NN periods. Refer to Fig. 3 for representation of lines and symbols.

suggested above using two theoretical understanding components: (i) coherent structures in neutral canopy flows [to understand the behavior of $R_{uu}(\mathbf{r};\Delta t)$ during the NN period D.e] and (ii) the influence of stable stratification on coherent structures [to understand the behavior of $R_{uu}(\mathbf{r};\Delta t)$ during TS periods].

(i) Coherent structures in neutral canopy flows

Turbulence in a tall canopy's vicinity is dominated by organized motions (or coherent structures; e.g., Denmead and Bradley 1985; Gao et al. 1989; Högström et al. 1989; Shaw et al. 1995, among numerous others). Finnigan et al. (2009)

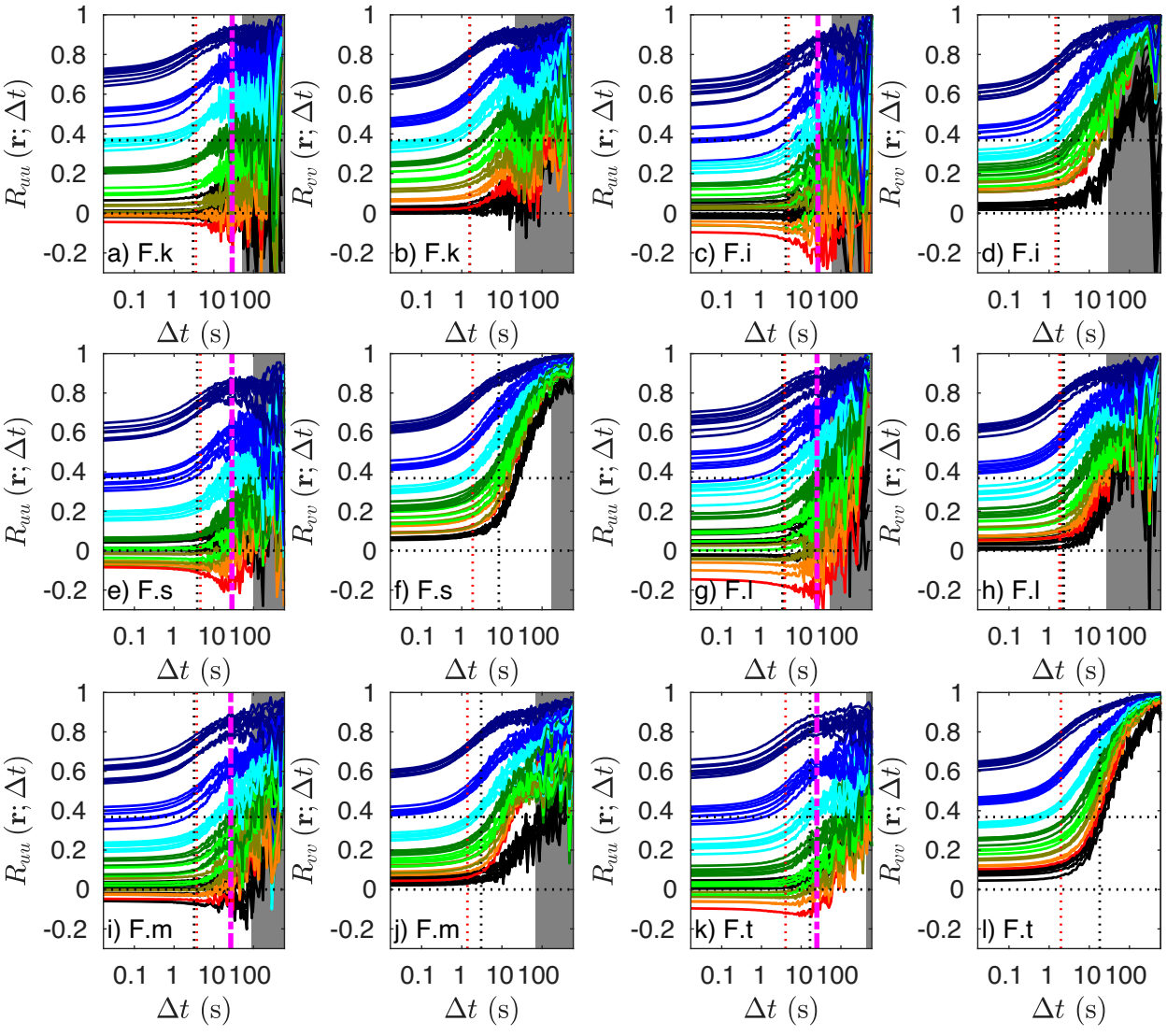

FIG. 6. The spatial autocorrelations of time-block-averaged streamwise and spanwise velocity fluctuations [$R_{uu}(\mathbf{r};\Delta t)$ (odd columns) and $R_{vv}(\mathbf{r};\Delta t)$ (even columns), respectively] during TS periods. In addition to representation of lines and symbols in Fig. 3, magenta vertical dashed–dotted lines annotate half of a buoyancy period. The buoyancy period is given by $2\pi/N$, where values of buoyancy frequency (N) are presented in Table 4.

used a novel composite averaging strategy to demonstrate from canopy-resolving LES that 3D canopy-scale coherent structures generally appear as superposed pairs of head-up and head-down hairpins [an updated version of the schematic diagram was provided by Patton and Finnigan (2013), Fig. 24.10]. The legs of such hairpins are streamwise-oriented vortical structures, which induce negative autocorrelations between w' at opposite spanwise locations with respect to the vortex cores. On average, the spanwise separation distances ($\mathbf{r}$) associated with negative correlations of w' are between half and one width of those hairpin legs. Because u' and w' are strongly correlated near the canopy top, negative autocorrelations of w' lead to negative autocorrelations of u' at such spanwise $\mathbf{r}$. As the value of $R_{uu}(\mathbf{r};\Delta t \to 0)$ varies from 1 at $\mathbf{r} = 0$ to a negative value at some spanwise $\mathbf{r}$, one expects a positive-to-negative transition of $R_{uu}(\mathbf{r};\Delta t \to 0)$ at a spanwise $\mathbf{r}$ comparable to the average spanwise location of those vortex cores with respect to the hairpin centerline. Given a mean wind direction of 198.6° during period D.e, the zonal direction is closely aligned with the spanwise direction, and the positive-to-negative transition of $R_{uu}(\mathbf{r};\Delta t \to 0)$ at a zonal separation distance of 10.32 m (approximately one canopy height, represented by olive colored curves in Fig. 5m) is consistent with previously reported spanwise locations of vortex cores [approximately 1.1 canopy heights from the hairpin centerline, suggested by LES results of Finnigan et al. (2009)] and positive-to-negative transitions of $R_{uu}(\mathbf{r};\Delta t \to 0)$ [at spanwise $\mathbf{r}$ of about 1.5 canopy heights, suggested by wind-tunnel data of Shaw et al. (1995) and LES

TABLE 4. Parameters estimated by performing a linear stability analysis of K-H instability development during TS periods shown in Fig. 6. The buoyancy frequency is calculated as $N = [(g/\overline{\theta}_v)(\Delta\overline{\theta}_v/\Delta z)]^{1/2}$, where $\Delta z = 1$ m is the difference between 10- and 11-m heights.

Period	$\Delta\overline{u}$ (m s^{-1})	N (s^{-1})	$k_{x,c}$ (m^{-1})	$\lambda_{x,c}$ (m)
F.i	0.49	0.13	0.15	43
F.k	0.51	0.11	0.08	75
F.l	0.53	0.15	0.15	41
F.m	0.53	0.14	0.13	49
F.s	0.51	0.13	0.14	45
F.t	0.52	0.15	0.18	36

results of Su et al. (2000)]. Here, we have made the connection between negative $R_{uu}(\mathbf{r} = 13.76$ m zonal; $\Delta t)$ during the NN period D.e to energy-containing coherent structures near the canopy top, which are characterized by integral length scales. For solely turbulent motions, motions on integral length scales are characterized by integral time scales, and the characteristic time scales of motions increase with their characteristic length scales. Thus, averaging fluctuations over an increasing Δt toward the integral time scale means removing an increasing amount of less-organized, relatively small-scale motions, which makes the influence of energy-containing coherent structures more evident, i.e., the negative $R_{uu}(\mathbf{r} = 13.76$ m zonal; $\Delta t)$ becomes increasingly negative. Further increasing Δt beyond the integral time scale means averaging an increasing number of coherent structures, which smooths out the influence of energy-containing coherent structures decreases, and correspondingly $R_{uu}(\mathbf{r} = 13.76$ m zonal; $\Delta t)$ becomes less negative and eventually increasingly positive.

(ii) Influence of stable stratification on coherent structures

In the presence of a stable stratification, the evolution of coherent structures in an x–z plane can be understood using the development of Kelvin–Helmholtz (K-H) instability in a mixing layer centered at the canopy top. Table 4 presents parameters estimated by performing a linear stability analysis. Specifically, a small vertical perturbation is expected to grow exponentially when the streamwise wavenumber (k_x) exceeds a critical number (Kundu et al. 2015, Chapter 11.3)

$$k_{x,c} = -\frac{2\Delta\overline{\rho}}{\overline{\rho}}\frac{g}{\Delta\overline{u}^2} \approx \frac{2\Delta\overline{\theta}_v}{\overline{\theta}_v}\frac{g}{\Delta\overline{u}^2}, \tag{9}$$

where $g = 9.81$ m s^{-2} is Earth's gravitational acceleration, ρ is the air density, and θ_v is the virtual potential temperature. Because correlations between data collected on the top beam of the array (at 10.6-m height) are of primary interest, vertical variations of physical quantities (represented by Δ) are estimated as close as possible to the height of 10.6 m by taking the difference between values measured at 11- and 10-m heights on the vertical tower.

Based on K-H linear stability analysis, structures with streamwise length scales smaller than $\lambda_{x,c}$ are dynamically unstable and will grow until their streamwise length scales become larger than $\lambda_{x,c}$, which then make them dynamically stable and arrests their growth. Consider the dynamical stability of energy-carrying coherent structures characterized by the longitudinal integral length scale of the streamwise velocity component ($\ell_{u,L}$). If $\lambda_{x,c} > 2\ell_{u,L}$, then most energy-containing coherent structures are dynamically unstable, meaning that the stable stratification induces only minor impacts on these structures. If $\lambda_{x,c} > 2\ell_{u,L}$, then a substantial portion of energy-containing coherent structures are dynamically stable, meaning that the stable stratification induces significant impacts on these structures.

Regarding the estimate of $\ell_{u,L}$, using the e-folding distance of $R_{uu}(\mathbf{r}; \Delta t \to 0)$ with r in the zonal direction is inappropriate because the zonal direction is closely aligned with the spanwise rather than the streamwise direction. Since direct estimates of $\ell_{u,L}$ from CHATS data are unavailable, we take the value from previously published laboratory experiment [Fig. 15 in Shaw et al. (1995), by directly integrating the longitudinal autocorrelation function] and LES [Fig. 12a in Patton et al. (2016), by detecting the e-folding distance of longitudinal autocorrelation function] of neutral canopy flows, where at canopy top $\ell_{u,L} \approx 3$ h. Here, "longitudinal autocorrelation" refers to the autocorrelation of streamwise velocity component between two points separated along the streamwise direction. This estimate of $\ell_{u,L}$ is fairly robust for neutral canopy flows with leaf area indices (LAIs) ranging from 0.47 [stalks in the wind-tunnel used by Shaw et al. (1995)] to 2 [forest simulated by Patton et al. (2016)], which should be reasonable for CHATS with LAIs ranging from 0.7 to 2.5 [reposted by Patton et al. (2011)]. Although the stable stratification is expected to reduce the size of coherent structures, such reduction does not affect the order of $\ell_{u,L}$ because the zonal separation at which the positive-to-negative transition of $R_{uu}(\mathbf{r}; \Delta t \to 0)$ occurs varies only from 10.32 to 8.6 m for periods available here (i.e., the NN period D.e and the TS periods).

Taking $\ell_{u,L} \approx 3\,\text{h} = 30\,\text{m}$, we obtain $\lambda_{x,c} < 2\ell_{u,L}$ during TS periods F.i, F.l, F.m, F.s, and F.t (when $z/\mathscr{L} \geq 0.069$), implying that most energy-containing coherent structures during these periods are dynamically stable. These stable structures propagate as internal gravity waves, where streamwise velocity fluctuations stay in phase over approximately half of a buoyancy period. As a result, the most negative $R_{uu}(\mathbf{r} = 13.76$ m zonal; $\Delta t)$ occurs at about half of a buoyancy period (red curves in Figs. 6c,e,l,m,t). For period F.k ($z/\mathscr{L} = 0.05$), $\lambda_{x,c} < 2\ell_{u,L}$, implying that most energy-containing coherent structures are dynamically unstable, although a small portion of coherent structures can be dynamically stable. Correspondingly, the most negative $R_{uu}(\mathbf{r} = 13.76$ m zonal; $\Delta t)$ occurs between the integral time scale and half of a buoyancy period (red curve in Fig. 6a).

In summary, the value of $\lambda_{x,c}$ relative to $2\ell_{u,L}$ suggests the stability of the energy-containing coherent structures, which then determines the location of the most negative $R_{uu}(\mathbf{r} = 13.76$ m zonal; $\Delta t)$ relative to the integral time scale and half of a buoyancy period. These results show that the 2D K-H instability development predicts the changes in the behaviors of $R_{uu}(\mathbf{r} = 13.76$ m zonal; $\Delta t)$ induced by a transition from NN to TS conditions reasonably well. Given the clear influence of stable stratification on the behaviors of $R_{uu}(\mathbf{r}; \Delta t)$ and nothing

unique in the behaviors of $R_{vv}(\mathbf{r}; \Delta t)$, the spatial autocorrelations of time-block-averaged fluctuations satisfy the expectation of a statistical measure capable of identifying nonturbulent motions caused by stable stratification (as discussed in section 2b).

3) Evaluating K-H instability parameters against nighttime wave dynamics derived from lidar images

In this subsection, we evaluate parameter values obtained in Table 4 against nighttime canopy-scale wave dynamics derived from aerosol backscatter lidar images collected during CHATS (Mayor 2017). Unfortunately, a case-by-case evaluation is unavailable because the aerosol backscatter lidar was not in operation during five of the six TS periods occurred [no data from 0330 UTC 15 May to 2100 UTC 19 May, as reported by Mayor (2010)], and the only TS period during which lidar images were sampled (F.m from 0654 to 0806 UTC 15 May) does not show any visible canopy-scale waves in lidar images [i.e., not identified by Mayor (2017)]. The absence of canopy-scale waves during period F.m is unsurprising because the negative $R_{uu}(\mathbf{r} = 13.76$ m zonal; $\Delta t \to 0)$ is statistically insignificant (>-0.05), implying an absence of sufficiently strong superposed pairs of head-up and head-down hairpins. Nevertheless, we can still perform an overall comparison between parameter values obtained in Table 4 and those presented in Table 1 of Mayor (2017). Specifically, the buoyancy frequencies (N) ranging from 0.11 to 0.15 s^{-1} in this work agree well with the most frequently observed wave periods ($\sim 2\pi/N$) between 40 and 60 s in Mayor (2017). The critical wavelengths ($\lambda_{x,c} = 2\pi/k_{x,c}$) ranging from 36 to 75 m in this work are within the reported wavelengths between 30 and 100 m in Mayor (2017). These results indicate that parameter values obtained for TS periods in this work fall within the ranges suggested by lidar images of nighttime canopy-scale wave dynamics.

4. Conclusions

a. *Summary of identified statistical signals of nonturbulent motions caused by stable stratification*

In this work, we investigate statistical signals of nonturbulent motions caused by stable stratification as opposed to solely turbulent motions. The scope focuses on near-surface flows where arrays of sonic anemometers can be deployed to resolve energy-containing motions in both space and time. Data from CHATS are selected for analysis not only because the deployment included 31 sonic anemometers but also because of the previously published aerosol backscatter lidar results of nighttime canopy-scale wave dynamics (Mayor 2017). Within the CHATS deployment, we select the "wide-high configuration" periods to investigate flows near the canopy top (where the influence of stratification is likely the strongest) using the widest range of horizontal sensor separations available.

The analysis procedures consist of two stages. In the first stage, we identify periods of statistically stationary, horizontally homogeneous, approximately 2D mean flows. The purpose of this stage is to limit the mechanism producing nonturbulent motions to stable stratification. The resulting periods are expected to contain solely turbulent motions for unstable conditions and a mixture of turbulent and internal gravity waves for stable conditions. Note that these "idealized" periods can also be used to improve the understanding of canopy flows for a wide range of stability conditions beyond the scope of this work.

In the second stage of analysis, we compare statistics carrying both spatial and temporal information during unstable and stable periods to identify signals of nonturbulent motions caused by stable stratification. The analysis is performed in a coordinate system that aligns with the mean wind direction. Instead of using the vertical velocity fluctuations (w'), which are directly affected by stable stratification, we use streamwise and spanwise velocity fluctuations (u' and v', respectively) for analysis. The purpose of using u' and v' is to reduce uncertainties associated with sonic tilts that can contaminate w'. A derivation of the momentum equation shows that signals of nonturbulent motions caused by stable stratification are expected from statistics of u' that is negatively correlated w', but not from statistics of v' that is uncorrelated with w'. Consequently, a statistical measure capable of identifying nonturbulent motions caused by stable stratification is expected to show unique behaviors for u', but not for v', under stable conditions compared to their behaviors under other conditions. Such expectation is observed from spatial autocorrelations of time-block-averaged fluctuations, where a transition from neutral to stable conditions leads to substantial changes in the behaviors of $R_{uu}(\mathbf{r}; \Delta t)$, but nothing unique in the behaviors of $R_{vv}(\mathbf{r}; \Delta t)$.

The physical base of signals of nonturbulent motions identified from the behaviors of $R_{uu}(\mathbf{r}; \Delta t)$ is examined both theoretically and practically. Theoretically, these nonturbulent motions caused by stable stratification are understood using existing knowledge of turbulent canopy flows and 2D K-H instability development. At the canopy top, coherent structures composed of superposed pairs of head-up and head-down hairpins lead to negative values of $R_{uu}(\mathbf{r}, \Delta t \to 0)$ at a zonal separation distance of 13.76 m. For neutral conditions, the average interval over which u' stays in phase is determined by the average lifetime of turbulent motions (i.e., the integral time scale), and therefore, $R_{uu}(\mathbf{r} = 13.76$ m zonal; $\Delta t)$ reaches a minimum as Δt approaches the integral time scale. For stable conditions, motions on streamwise length scales larger than a critical wavelength ($\lambda_{x,c}$) are stable, and the associated u' stays in phase over half of a buoyancy period. As the stratification increases and the flow becomes sufficiently stable ($z/\mathscr{L} \geq 0.069$), $\lambda_{x,c}$ becomes shorter than twice of the longitudinal integral length scale of streamwise velocity ($\ell_{u,L}$), making most flux-carrying coherent structures stable. In such cases, $R_{uu}(\mathbf{r} = 13.76$ m zonal; $\Delta t)$ reaches a minimum as Δt approaches half of a buoyancy period, which is typically an order of magnitude larger than the integral time scale. Practically, estimates of $\lambda_{x,c}$ and buoyancy periods agree well with the overall environmental and wave properties during periods of nighttime canopy-scale waves visually identified from lidar images (Mayor 2017). The understanding of coherent structures in canopy flows influenced by stable stratification

obtained in this work adds to the existing knowledge of stability effects on coherent structures obtained for other flows (e.g., Carper and Porté-Agel 2004; Li and Bou-Zeid 2011; Harikrishnan et al. 2023).

In addition to the spatial autocorrelations of time-block-averaged fluctuations, we have also tried other statistics carrying both spatial and temporal information, like the cumulative integrals of Fourier cospectra of fluctuations at separated locations. Results of neither $O_{uu}(\mathbf{r}; f)$ nor $O_{vv}(\mathbf{r}; f)$ show any unique behavior under stable conditions, implying no detection of nonturbulent motions. A key difference between $O_{\phi\phi}(\mathbf{r}; f)$ and $R_{\phi\phi}(\mathbf{r}; \Delta t)$ is that the former represents the contribution of motions at a frequency of f and higher to the two-point covariance, whereas the latter represents the contribution of motions at a time scale Δt and larger to the coherence between two points. While motions on a certain length scale ($\mathbf{r}$) can influence the coherence between two points separated by up to a few times of $\mathbf{r}$, they contribute little to the covariance of fluctuations at two points separated by $\mathbf{r}$ or larger. Given the energy-containing coherent structures influenced by stable stratification (discussed above), one can search for signals of nonturbulent motions within a larger range of r from $R_{uu}(\mathbf{r}; \Delta t)$ results, as compared to $O_{uu}(\mathbf{r}; f)$ results. Thus, $R_{uu}(\mathbf{r}; \Delta t)$ has a better chance of capturing signals of nonturbulent motions caused by stable stratification than $O_{uu}(\mathbf{r}; f)$.

Before finishing this subsection, we also discuss the appropriateness of estimating mean wind direction using data collected by the sensor at the canopy top on the tower [as mentioned in section 2b(2)]. For each period used to obtain statistical results in section 3b, the canopy-top mean wind directions at the tower location can be up to 8° different from those at the array location (Table 3, with period D.b being excluded). Regarding signals of nonturbulent motions identified from $R_{uu}(\mathbf{r}; \Delta t)$, previous wind-tunnel data of neutral canopy flows suggest that a difference up to 8° has negligible influence on estimates of spatial correlations of u' (Shaw et al. 1995, Fig. 14). Regarding the absence of signals of nonturbulent motions in $O_{uu}(\mathbf{r}; f)$ results, these uncertainties in mean wind directions are unimportant either. Thus, uncertainties in mean wind direction estimates are unlikely to influence the major findings in this work.

b. *Implications on LES of stably stratified near-surface atmospheric flows*

A persistent challenge faced by noncanopy-resolving LES is the inability to resolve the energy-containing motions at the lowest few grid levels. When energy-containing motions are underresolved, the subgrid-scale (SGS) model can no longer assume "universal" behaviors of SGS turbulent motions. Previous studies have explored various approaches of reproducing the underresolved near-surface turbulence for neutral and unstable conditions, including SGS models (e.g., Sullivan et al. 1994; Bou-Zeid et al. 2005; Chow et al. 2005), bottom boundary conditions (e.g., Bou-Zeid et al. 2005; Kawai and Larsson 2012; Yang et al. 2017), additional sources of surface stresses (e.g., Chow et al. 2005), and advection schemes (e.g., Wang et al. 2021). Proposing methods to capture the influence of stable stratification on underresolved energy-containing motions near surface remains an ongoing effort for noncanopy-resolving LES (e.g., McWilliams et al. 2023). In this work, the agreement between 2D K-H instability predictions and the behaviors of $R_{uu}(\mathbf{r} = 13.76$ m zonal; $\Delta t)$ suggests potential advantages for understanding the dynamics of stably stratified ABL using canopy-resolving LES. As explained in section 3b, the 2D K-H instability analysis suggests that motions on scales smaller than $\lambda_{x,c}$ are unstable, implying that they still undergo free instability development as if the stable stratification is absent. Thus, as long as a canopy-resolving LES also resolves $\lambda_{x,c}$, SGS turbulent motions can be considered as universal and hence leaving the influence of stable stratification on SGS fluxes unimportant. Results from such canopy-resolving LES runs can then be used to understand 3D interactions between turbulent and wave motions, evaluate assumptions employed by existing analytical models (e.g., the 2D K-H instability analysis), explain differences between analytical model predictions and observations [e.g., phase angle differences between u' and w' shown in Fig. 5 in Lee (1997)], and develop SGS models for noncanopy-resolving LES runs.

The two-point statistics computed in this work also provide valuable metrics for evaluating canopy-resolving LES. Proper estimates of these two-point ensemble-averaged statistics are ensured by using flow-dependent identification of stationary periods (i.e., by using a technique such as MSATv2, as verified in appendix B) as well as other stringent criteria. The ability to reproduce $R_{uu}(\mathbf{r}; \Delta t)$ can be used as a criterion to examine LES runs of stably stratified canopy flows.

Acknowledgments. This work was supported by the National Science Foundation (Y. P. and S. C. W., Award AGS-2113854; E. G. P., NSF NCAR's Mesoscale and Microscale Meteorology Laboratory and Geophysical Turbulence Program under Cooperative Agreement 1852977). We thank Chad Bahrmann, Chuck Pavloski, and the College of Earth and Mineral Sciences' IT Support Group at Penn State for building and maintaining the computational environment used to conduct this work. We acknowledge Chuyue Xie for preliminary exercising of applying MSATv2 to CHATS data during the foliated phase. We acknowledge Natasha Miles and Colin Zarzycki for providing feedback on the analysis of results and an earlier draft of this paper. We would like to acknowledge the operational and technical and scientific support provided by NCAR's Earth Observing Laboratory (particularly, Steven Oncley for providing access to the raw CHATS data). We thank the Cilker family for allowing CHATS to be conducted in their orchard. We also thank the editor Peter Bertello and three anonymous reviewers for their constructive comments to help us improve this manuscript. Components of the results presented here were included in a paper with different objectives that was previously submitted to Journal of Fluid Mechanics (JFM); we thank JFM editors Charles Meneveau and Ivan Marusic as well as three anonymous reviewers for constructive comments and criticism.

Data availability statement. All data and numerical code supporting the findings of this work are openly available at the Penn State DataCommons (https://doi.org/10.26208/JY60-KN43). We thank Bernd Haupt for help us with publishing the data.

APPENDIX A

Procedures to Identify Periods of Statistically Stationary, Horizontally Homogeneous, Approximately 2D Mean Flows

a. Before stationarity analysis: Preparing continuous data-collecting periods

To begin analysis procedures in Fig. 2, all CSAT3 data have undergone transducer shadowing correction following Horst et al. (2015) and missing-value interrogation. The missing values include periods during which a sensor was out of operation and unphysical values annotated by nonzero CSAT3 diagnostic codes. Most of the "wide–high configuration" periods are covered by five periods of 20 h or longer during which all 13 sonic anemometers on the tower were operating continuously: (i) from 2212 UTC 31 March to 0121 UTC 3 April (51.15 h), (ii) from 0124 UTC 3 April to 1651 UTC 5 April (63.45 h), (iii) from 2233 UTC 13 May to 1900 UTC 14 May (20.45 h), (iv) from 2000 UTC 14 May to 1839 UTC 15 May (22.65 h), and (v) from 1842 UTC 15 May to 1827 UTC 17 May (47.75 h). Periods during which all 18 sonic anemometers on the array were operating continuously are relatively short, with only five periods of 10 h or longer: (i) from 1803 UTC 1 April to 0530 UTC 2 April (11.45 h), (ii) from 1627 UTC 3 April to 1057 UTC 4 April (18.5 h), (iii) from 0503 UTC 14 May to 1706 UTC 14 May (12.05 h), (iv) from 1842 UTC 15 May to 2127 UTC 16 May (26.75 h), and (v) from 2130 UTC 16 May to 1357 UTC 17 May (16.45 h).

b. Stationarity analysis: Identifying periods of stationary mean wind field using MSATv2

In this work, periods of stationary mean wind field are identified using MSATv2 [see flowchart in Pan and Patton (2020), Fig. 1]. The most important advantage of selecting MSATv2 rather than other existing stationarity analysis techniques is that we do not need to presume a uniform length of stationary periods. Given a continuous data-collecting period, MSATv2 takes all three velocity components averaged over blocks of δt as inputs, evaluates the stationarity of each possible time series of $10\delta t$ or longer, and then identifies the occurrence of nonstationary events if two consecutive inputs that can never belong to any stationary time series. The stationarity of each velocity component during each possible period is evaluated using the reverse arrangement test (RAT; Kendall et al. 1979), which is most suitable for analyzing near-surface wind field [explained in detail by Pan and Patton (2017)]. By evaluating all possible periods of $10\delta t$ or longer, MSATv2 takes into account flow-dependent time scales during the given data-collecting period.

For midlatitude ABLs that experience clear diurnal cycles, having continuous data-collecting periods of about 24 h or longer is critical for applying MSATv2 to near-surface sonic anemometer data. For CHATS data, one would like to take advantage of the substantially longer continuous data-collecting periods at the tower location than those at the array location, while flow behaviors at the array location are also accounted for. Thus, MSATv2 is first applied to data collected by 13 sensors on the tower during the associated five continuous periods of 20 h or longer to determine statistically stationary periods. Afterward, MSATv2 is applied to data collected by 18 sensors on the array during the associated five continuous periods of 10 h or longer to check the possible presence of nonstationary events. All other periods during which all 18 sensors on the array were operating continuously are too short for MSATv2 to yield statistically robust results. Each stationary period determined using tower data is marked as "yes" or "no" depending on whether nonstationary events are present at the array location, or as "unknown" when statistically robust MSATv2 results are unavailable at the array location (see Tables 1 and 2). Compared to synthesizing the stationarity of time series collected by all 31 sensors equitably, the current approach weighs tower data more importantly than array data. Such uneven weighting is physically appropriate as near-surface flow statistics (including stationarity) vary most profoundly in the vertical direction (Wyngaard 2010, p. 196). In other words, one can expect tower data collected at 13 heights to capture the most essential temporal variability in the flow field.

When using MSATv2 to determine statistically stationary periods, one needs to specify two key parameters for the stationarity test: (i) the averaging time block (δt) used to obtain inputs and (ii) the significance level (α) specified for RAT. Increasing α specified to RAT means becoming increasingly stringent when identifying statistically stationary periods. In addition, because RAT measures are robust only when inputs are approximately independent from each other, a resulting stationary period is only reliable when integral time scales of all three velocity components are less than $\delta t/2$. Thus, for a given δt, an optimal choice of α is expected to yield a maximum number of reliable stationary periods suitable for answering the scientific question of interest.

c. After stationarity analysis: Keeping only periods of horizontally homogeneous mean wind

Here, each period of stationary mean wind field is examined for horizontal homogeneity in two steps. The first step is to keep only periods of southerly mean winds to guarantee ample fetch of the orchard canopy. The second step is to examine whether the mean flow is approximately 2D by comparing mean wind directions across array and tower sensors at the same height.

APPENDIX B

Nonstationary Events Identified Using MSATv2: Capturing Changes in Characteristic Scales

Among the stationary south-wind periods identified in section 3a, applying MSATv2 to array data identifies nonstationary events during periods D.c and F.i. Visual inspection of 3-min averaged velocity time series measured by the canopy-top tower sensor and nine array sensors on the top beam suggests that period D.c (0003–0100 UTC 2 April) immediately follows a change in wind direction from approximately south (before 2300 UTC 1 April) to approximately west (between 2300 UTC 1 April and 0000 UTC 2 April) and then to southwest (after 0000 UTC 2 April; see Fig. B1), while period F.i (0600–0630 UTC 16 May) immediately follows a change in wind direction from southwest (before 0600 UTC 16 May) to approximately south (after 0600 UTC 16 May, see Fig. B2). These nonstationary events at the array location during periods D.c and F.i are likely the tails of dynamic transitions happening at both array and tower locations.

The nonstationary events in Figs. B1 and B2 have successfully captured the changes in the characteristic scales of turbulent motions, as revealed by the abrupt changes in the variation of 3-min averaged velocity time series across sensors. In Fig. B1, time series measured by nine array sensors show negligible spread before 2300 UTC 1 April but nonnegligible spread after 0000 UTC 2 April. In Fig. B2, time series measured by nine array sensors show nonnegligible spread before 1200 UTC 16 May but negligible spread after 1500 UTC 16 May. Recall that statistically stationary periods are determined using $\delta t \leq 6$ min, where δt is at least twice of the integral time scale. Thus, 3-min averaged velocity time series show motions on scales comparable to or larger than integral scales. A negligible spread of time series across nine array sensors often corresponds to tower data outside the spread, implying that 3-min averaged velocities are insensitive to a change in horizontal location of 1.72–13.76 m but sensitive to a change in horizontal location of 116 m. In such situation, turbulent motions are likely characterized by length scales on the order of 100 m, consistent with the expectation of ABL-scale motions during these relatively weak-wind daytime periods (e.g., before 2300 UTC 1 April in Fig. B1 and after 1500 UTC 16 May in Fig. B2). A nonnegligible spread of time series across nine array sensors often corresponds to tower data within the spread, implying that 3-min averaged velocities are sensitive to a change in horizontal location of 1.72–13.76 m but insensitive to a change in horizontal location of 116 m. In such situation, turbulent motions are likely characterized by length scales on the order of 10 m, consistent with the expectation of canopy-scale motions during these nighttime and relatively strong-wind daytime periods (e.g., before 0000 UTC 2 April in Fig. B1 and before 1200 UTC 16 May in Fig. B2). The capability of capturing changes in the characteristic scales of turbulent motions demonstrates the

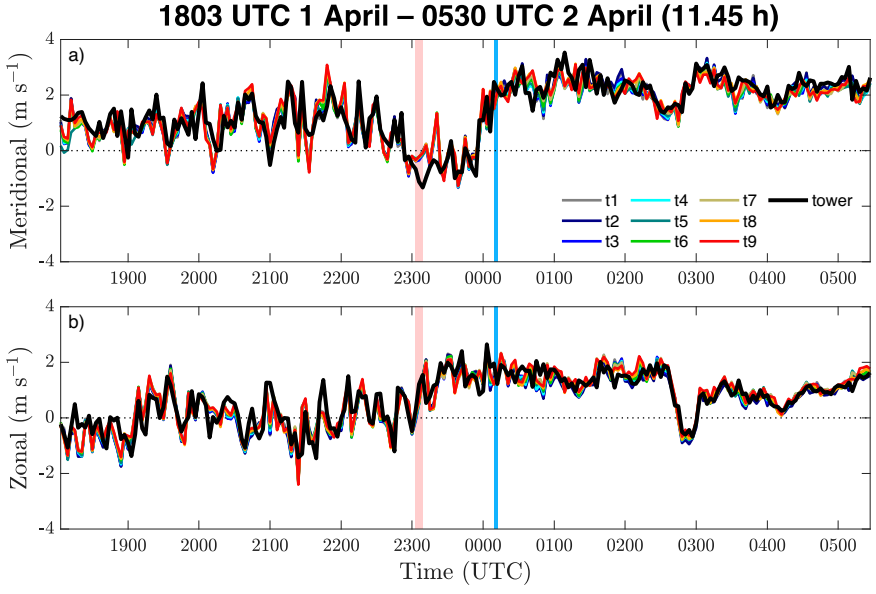

FIG. B1. Time series of 3-min averaged meridional and zonal velocity components measured using nine sensors on the top beam of the array (solid lines of various colors) and the canopy-top tower sensor (the black dotted line) during 1803 UTC 1 Apr–0530 UTC 2 Apr. The red vertical stripe represents the nonstationary event determined by applying MSATv2 with $\alpha = 0.05$ to 3-min averaged velocity components measured using 13 sensors on the tower: 2303–2309 UTC 1 Apr. The blue stripe represents the nonstationary event determined by applying MSATv2 with $\alpha = 0.05$ to 3-min averaged velocity components measured using 18 sensors on the array: 0009–0012 UTC 2 Apr.

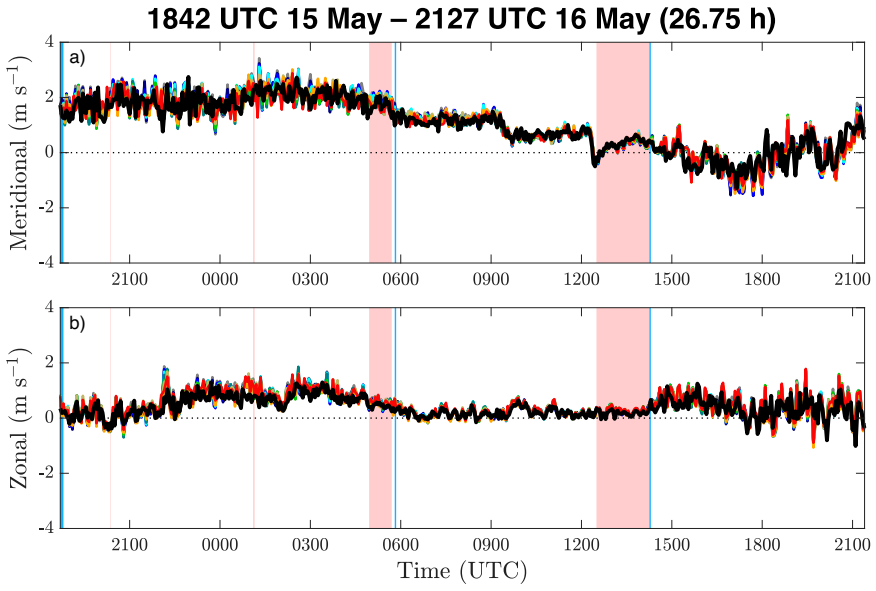

FIG. B2. Time series of 3-min averaged meridional and zonal velocity components measured using nine sensors on the top beam of the array and the canopy-top tower sensor during 1842 UTC 15 May–2127 UTC 16 May (refer to Fig. B1 for representation of lines). The red vertical stripes represent nonstationary events determined by applying MSATv2 with $\alpha = 0.10$ to 3-min averaged velocity components measured using 13 sensors on the tower: 2021 UTC 15 May, 0106–0109 UTC 16 May, 0457–0542 UTC 16 May, and 1230–1415 UTC 16 May. The blue stripes represent nonstationary events determined by applying MSATv2 with $\alpha = 0.10$ to 3-min averaged velocity components measured using 18 sensors on the array: 1842–1848 UTC 16 May, 0548–0551 UTC 16 May, and 1415–1418 UTC 16 May.

advantage of using MSATv2 that accounts for flow-dependent time scales.

REFERENCES

Beare, R. J., and Coauthors, 2006: An intercomparison of large-eddy simulations of the stable boundary layer. *Bound.-Layer Meteor.*, **118**, 247–272, https://doi.org/10.1007/s10546-004-2820-6.

Bou-Zeid, E., C. Meneveau, and M. Parlange, 2005: A scale-dependent Lagrangian dynamic model for large eddy simulation of complex turbulent flows. *Phys. Fluids*, **17**, 025105, https://doi.org/10.1063/1.1839152.

Carper, M. A., and F. Porté-Agel, 2004: The role of coherent structures in subfilter-scale dissipation of turbulence measured in the atmospheric surface layer. *J. Turbul.*, **5**, 040, https://doi.org/10.1088/1468-5248/5/1/040.

Chow, F. K., R. L. Street, M. Xue, and J. H. Ferziger, 2005: Explicit filtering and reconstruction turbulence modeling for large-eddy simulation of neutral boundary layer flow. *J. Atmos. Sci.*, **62**, 2058–2077, https://doi.org/10.1175/JAS3456.1.

Cook, P. A., and I. A. Renfrew, 2015: Aircraft-based observations of air–sea turbulent fluxes around the British Isles. *Quart. J. Roy. Meteor. Soc.*, **141**, 139–152, https://doi.org/10.1002/qj.2345.

Davidson, P. A., 2015: *Turbulence: An Introduction for Scientists and Engineers.* 2nd ed. Oxford University Press, 630 pp., https://doi.org/10.1093/acprof:oso/9780198722588.001.0001.

Denmead, O. T., and E. F. Bradley, 1985: Flux-gradient relationships in a forest canopy. *The Forest-Atmosphere Interaction*, B. A. Hutchison and B. B. Hicks, Eds., Springer, 421–442, https://doi.org/10.1007/978-94-009-5305-5_27.

Dupont, S., and E. G. Patton, 2012: Influence of stability and seasonal canopy changes on micrometeorology within and above an orchard canopy: The CHATS experiment. *Agric. For. Meteor.*, **157**, 11–29, https://doi.org/10.1016/j.agrformet.2012.01.011.

Finnigan, J. J., R. H. Shaw, and E. G. Patton, 2009: Turbulence structure above a vegetation canopy. *J. Fluid Mech.*, **637**, 387–424, https://doi.org/10.1017/S0022112009990589.

French, J. R., W. M. Drennan, J. A. Zhang, and P. G. Black, 2007: Turbulent fluxes in the hurricane boundary layer. Part I: Momentum flux. *J. Atmos. Sci.*, **64**, 1089–1102, https://doi.org/10.1175/JAS3887.1.

Gao, W., R. H. Shaw, and K. T. Paw U, 1989: Observation of organized structure in turbulent flow within and above a forest canopy. *Bound.-Layer Meteor.*, **47**, 349–377, https://doi.org/10.1007/BF00122339.

Harikrishnan, A., M. Rodal, R. Klein, D. Margerit, and N. Vercauteren, 2023: On the motion of hairpin filaments in the atmospheric boundary layer. *Phys. Fluids*, **35**, 076063, https://doi.org/10.1063/5.0151078.

Högström, U., H. Bergström, A.-S. Smedman, S. Halldin, and A. Lindroth, 1989: Turbulent exchange above a pine forest, I: Fluxes and gradients. *Bound.-Layer Meteor.*, **49**, 197–217, https://doi.org/10.1007/BF00116411.

Horst, T. W., S. R. Semmer, and G. Maclean, 2015: Correction of a non-orthogonal, three-component sonic anemometer for flow distortion by transducer shadowing. *Bound.-Layer Meteor.*, **155**, 371–395, https://doi.org/10.1007/s10546-015-0010-3.

Kawai, S., and J. Larsson, 2012: Wall-modeling in large eddy simulation: Length scales, grid resolution, and accuracy. *Phys. Fluids*, **24**, 015015, https://doi.org/10.1063/1.3678331.

Kendall, M. G., A. Stuart, and J. K. Ord, 1979: *The Advanced Theory of Statistics.* Vol. 2. Macmillan Publishing Co. Inc., 748 pp.

Kundu, P. K., I. M. Cohen, and D. R. Dowling, 2015: *Fluid Mechanics.* Academic Press, 928 pp., https://doi.org/10.1016/C2012-0-00611-4.

Lee, X., 1997: Gravity waves in a forest: A linear analysis. *J. Atmos. Sci.*, **54**, 2574–2585, https://doi.org/10.1175/1520-0469(1997)054<2574:GWIAFA>2.0.CO;2.

LeMone, M. A., and Coauthors, 2019: 100 years of progress in boundary layer meteorology. *A Century of Progress in Atmospheric and Related Sciences: Celebrating the American Meteorological Society Centennial*, *Meteor. Monogr.*, No. 59, Amer. Meteor. Soc., https://doi.org/10.1175/AMSMONOGRAPHS-D-18-0013.1.

Li, D., and E. Bou-Zeid, 2011: Coherent structures and the dissimilarity of turbulent transport of momentum and scalars in the unstable atmospheric surface layer. *Bound.-Layer Meteor.*, **140**, 243–262, https://doi.org/10.1007/s10546-011-9613-5.

Lloyd, C. J., R. M. Dorrell, and C. P. Caulfield, 2022: The coupled dynamics of internal waves and hairpin vortices in stratified plane Poiseuille flow. *J. Fluid Mech.*, **934**, A10, https://doi.org/10.1017/jfm.2021.1007.

Lumley, J. L., and H. S. Panofsky, 1964: *The Structure of Atmospheric Turbulence.* John Wiley and Sons, Inc., 239 pp.

Mahrt, L., 2014: Stably stratified atmospheric boundary layers. *Annu. Rev. Fluid Mech.*, **46**, 23–45, https://doi.org/10.1146/annurev-fluid-010313-141354.

Mayor, S. D., 2010: Raman-shifted Eye-safe Aerosol Lidar (REAL) scan images and time-lapse animations from the Canopy Horizontal Array Turbulence Study (CHATS). California State University Chico, accessed 4 April 2024, https://lidar.csuchico.edu/lgd/nsf_results/.

——, 2017: Observations of microscale internal gravity waves in very stable atmospheric boundary layers over an orchard canopy. *Agric. For. Meteor.*, **244–245**, 136–150, https://doi.org/10.1016/j.agrformet.2017.05.014.

McWilliams, J. C., C. Meneveau, E. G. Patton, and P. P. Sullivan, 2023: Stable boundary layers and subfilter-scale motions. *Atmosphere*, **14**, 1107, https://doi.org/10.3390/atmos14071107.

Oncley, S. P., C. A. Friehe, J. C. Larue, J. A. Businger, E. C. Itsweire, and S. S. Chang, 1996: Surface-layer fluxes, profiles, and turbulence measurements over uniform terrain under near-neutral conditions. *J. Atmos. Sci.*, **53**, 1029–1044, https://doi.org/10.1175/1520-0469(1996)053<1029:SLFPAT>2.0.CO;2.

Pan, Y., and E. G. Patton, 2017: On determining stationary periods within time series. *J. Atmos. Oceanic Technol.*, **34**, 2213–2232, https://doi.org/10.1175/JTECH-D-17-0038.1.

——, and ——, 2020: Determining stationary periods across multiple sensors: An application to observed canopy turbulence response to atmospheric stability. *J. Atmos. Oceanic Technol.*, **37**, 665–685, https://doi.org/10.1175/JTECH-D-19-0135.1.

Patton, E. G., and J. J. Finnigan, 2013: Canopy turbulence. *Handbook of Environmental Fluid Dynamics*, H. J. S. Fernando, Ed., Vol. 1, CRC Press, 311–327, https://doi.org/10.1201/b14241.

——, and Coauthors, 2011: The canopy horizontal array turbulence study. *Bull. Amer. Meteor. Soc.*, **92**, 593–611, https://doi.org/10.1175/2010BAMS2614.1.

——, P. P. Sullivan, R. H. Shaw, J. J. Finnigan, and J. C. Weil, 2016: Atmospheric stability influences on coupled boundary layer and canopy turbulence. *J. Atmos. Sci.*, **73**, 1621–1647, https://doi.org/10.1175/JAS-D-15-0068.1.

Raupach, M. R., and R. H. Shaw, 1982: Averaging procedures for flow within vegetation canopies. *Bound.-Layer Meteor.*, **22**, 79–90, https://doi.org/10.1007/BF00128057.

Riley, J. J., and M.-P. Lelong, 2000: Fluid motions in the presence of strong stable stratification. *Annu. Rev. Fluid Mech.*, **32**, 613–657, https://doi.org/10.1146/annurev.fluid.32.1.613.

Shaw, R. H., Y. Brunet, J. J. Finnigan, and M. R. Raupach, 1995: A wind tunnel study of air flow in waving wheat: Two-point velocity statistics. *Bound.-Layer Meteor.*, **76**, 349–376, https://doi.org/10.1007/BF00709238.

Su, H.-B., R. H. Shaw, and K. T. Paw U, 2000: Two-point correlation analysis of neutrally stratified flow within and above a forest from large-eddy simulation. *Bound.-Layer Meteor.*, **94**, 423–460, https://doi.org/10.1023/A:1002430213742.

Sullivan, P. P., J. C. McWilliams, and C.-H. Moeng, 1994: A subgrid-scale model for large-eddy simulation of planetary boundary-layer flows. *Bound.-Layer Meteor.*, **71**, 247–276, https://doi.org/10.1007/BF00713741.

——, J. C. Weil, E. G. Patton, H. J. J. Jonker, and D. V. Mironov, 2016: Turbulent winds and temperature fronts in large-eddy simulations of the stable atmospheric boundary layer. *J. Atmos. Sci.*, **73**, 1815–1840, https://doi.org/10.1175/JAS-D-15-0339.1.

Sun, J., and Coauthors, 2015: Review of wave-turbulence interactions in the stable atmospheric boundary layer. *Rev. Geophys.*, **53**, 956–993, https://doi.org/10.1002/2015RG000487.

UCAR/NCAR–Earth Observing Laboratory, 2011: ISFF high rate tower data, version 1.0. UCAR/NCAR, accessed 28 February 2017, https://doi.org/10.5065/D67S7KZ8.

Vercauteren, N., L. Mahrt, and R. Klein, 2016: Investigation of interactions between scales of motion in the stable boundary layer. *Quart. J. Roy. Meteor. Soc.*, **142**, 2424–2433, https://doi.org/10.1002/qj.2835.

Vickers, D., and L. Mahrt, 2003: The cospectral gap and turbulent flux calculations. *J. Atmos. Oceanic Technol.*, **20**, 660–672, https://doi.org/10.1175/1520-0426(2003)20<660:TCGATF>2.0.CO;2.

——, and ——, 2006a: Contrasting mean vertical motion from tilt correction methods and mass continuity. *Agric. For. Meteor.*, **138**, 93–103, https://doi.org/10.1016/j.agrformet.2006.04.001.

——, and ——, 2006b: A solution for flux contamination by mesoscale motions with very weak turbulence. *Bound.-Layer Meteor.*, **118**, 431–447, https://doi.org/10.1007/s10546-005-9003-y.

Wang, A., Y. Pan, and P. M. Markowski, 2021: The influence of WENO schemes on large-eddy simulations of a neutral atmospheric boundary layer. *J. Atmos. Sci.*, **78**, 3613–3628, https://doi.org/10.1175/JAS-D-21-0033.1.

Wyngaard, J. C., 2010: *Turbulence in the Atmosphere.* Cambridge University Press, 393 pp., https://doi.org/10.1017/CBO9780511840524.

Yang, X. I. A., G. I. Park, and P. Moin, 2017: Log-layer mismatch and modeling of the fluctuating wall stress in wall-modeled large-eddy simulations. *Phys. Rev. Fluids.*, **2**, 104601, https://doi.org/10.1103/PhysRevFluids.2.104601.

Zou, Z., D. Zhao, B. Liu, J. A. Zhang, and J. Huang, 2017: Observation-based parameterization of air-sea fluxes in terms of wind speed and atmospheric stability under low-to-moderate wind conditions. *J. Geophys. Res. Oceans*, **122**, 4123–4142, https://doi.org/10.1002/2016JC012399.